A model study of Saharan dust emissions and distributions during the SAMUM-1 campaign

B. Laurent,[1,2] I. Tegen,[1] B. Heinold,[1] K. Schepanski,[1,3] B. Weinzierl,[4] and M. Esselborn[4,5]

Received 11 August 2009; revised 30 June 2010; accepted 8 July 2010; published 12 November 2010.

[1] Simulations of Saharan dust emission, transport, and deposition are performed using new developments of the regional model COSMO-MUSCAT for the Saharan Mineral Dust Experiment (SAMUM-1), which took place in May–June 2006. Up-to-date surface soil data sets developed especially to model dust emissions are used, and a new representation of the dust size distribution is proposed. Compared with previous model studies performed with COSMO-MUSCAT, the advantage of our approach is that no tuning factor on the erosion threshold is needed for the whole Sahara. The performances and limitations of COSMO-MUSCAT to model the regional dust cycle are discussed. The spatiotemporal variability of simulated Saharan emissions is evaluated using a backtracking approach to locate dust sources with Meteosat Second Generation (MSG) infrared difference images and using dust observations of North African meteorological stations. The Saharan dust emissions are estimated to be 78 Tg during the studied period. The model dust size distributions agree well with SAMUM-1 airborne measurements, previous model simulations, and Aerosol Robotic Network (AERONET) inversion products. Our ability to simulate the vertical cross section of a dust plume is also discussed with regard to airborne lidar measurements and former simulations. The horizontal distribution of model-derived aerosol optical thicknesses (AOT) is compared with Aqua-MODIS Deep Blue AOT and Ozone Monitoring Instrument (OMI) aerosol indexes. Dry and wet deposition rates are simulated. About 67% of the emitted dust is deposited in the vicinity of the emitted source areas over North Africa and close marine areas, and 33% is transported out of the studied area toward other continents and remote ocean areas.

Citation: Laurent, B., I. Tegen, B. Heinold, K. Schepanski, B. Weinzierl, and M. Esselborn (2010), A model study of Saharan dust emissions and distributions during the SAMUM-1 campaign, *J. Geophys. Res.*, *115*, D21210, doi:10.1029/2009JD012995.

1. Introduction

[2] Atmospheric mineral dust is mainly produced by aeolian erosion acting in arid and semiarid areas. Mineral dust has an impact on the Earth's radiative budget by absorbing and scattering incoming solar and outgoing terrestrial radiations [*Sokolik and Toon*, 1999]. Mineral dust is involved in heterogeneous and multiphase atmospheric chemistry, affecting photo-oxidant concentrations and the composition of precipitation [*Loÿe-Pilot et al.*, 1986; *Losno et al.*, 1991; *Bauer et al.*, 2004]. It also contributes to the biogeochemical cycles of many elements, and in particular those of nutrients such as Fe and P for remote oceans and the Amazon forest [*Bergametti et al.*, 1992; *Swap et al.*, 1992; *Jickells et al.*, 2005].

[3] To forecast dust events and predict changes under different climate conditions, a good understanding of the emission processes and the characteristics of source regions is essential. To evaluate the radiative and biogeochemical impacts due to mineral dust and the risks for the exposed populations living close to the source areas, dust concentration fields and their properties have to be determined precisely. Dust events are highly variable in space and time, and their composition is closely connected to their emitted source areas and to their production processes. Moreover, the limited number of existing field measurements of dust events is not sufficient to constrain realistic estimates of dust loads and their properties.

[4] Intensive experimental campaigns and modeling studies are essential to investigate the dust cycle and the environmental impacts from local to regional scales. The first phase of the Saharan Mineral Dust Experiment (SAMUM-1) was carried out in Morocco from 12 May to 7 June 2006. One of the aims of this project was to clarify uncertainties in radiative properties of dust. Dust characteristics determined from ground-based, airborne, and spaceborne remote sensing, as

[1]Leibniz-Institut für Troposhärenforschung, Leipzig, Germany.
[2]Now at Laboratoire Interuniversitaire des Systèmes Atmosphériques, Créteil, France.
[3]Now at Institute for Atmospheric Science, School of Earth and Environment, University of Leeds, Leeds, UK.
[4]Deutsches Zentrum für Luft- und Raumfahrt, Institut für Physik der Atmosphäre, Oberpfaffenhofen, Germany.
[5]Now at European Southern Observatory, Garching, Germany.

0148-0227/10/2009JD012995

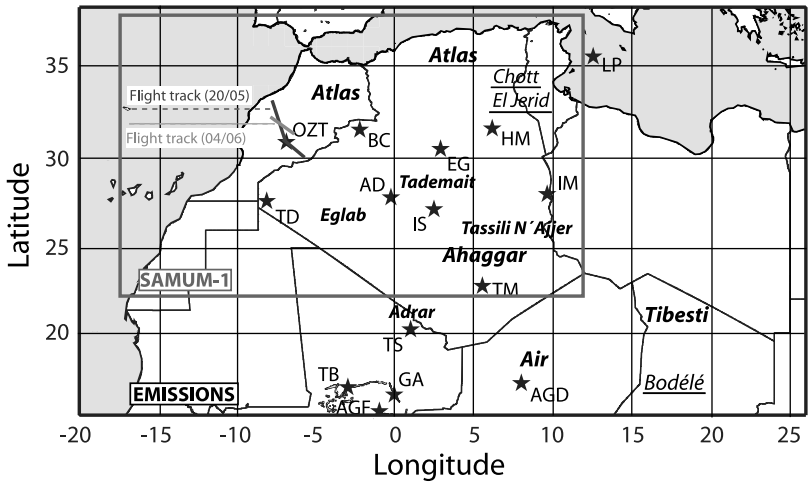

Figure 1. COSMO-MUSCAT simulation domain for Saharan dust emissions (extending from 16°N to 38°N and from 19°W to 27°E), and a SAMUM-1 area with the location of observation sites (Ouarzazate, OZT; Béchar, BC; El Goléa, EG; Hassi Messaoud, HM; Lampedusa, LP; Tindouf, TD; Adrar, AD; In Salah, IS; In Amenas, IM; Tamanrasset, TM; Tessalit, TS; Toubouctou, TB; Agoufou, AGF; Gao, GA; Agadez, AGD) and the two Falcon flight tracks presented in Figure 8.

well as analyzed microphysical, chemical, and morphological properties of dust aerosol from field samples, were measured [*Heintzenberg*, 2009]. The SAMUM-1 experiment was concentrated in the ground stations of Ouarzazate (30.9°N, 6.9°W) and Tinfou near Zagora (30.2°N, 5.6°W). As described by *Heintzenberg* [2009], research aircraft measured solar spectral irradiances and surface albedo or provided in situ physical aerosol measurements and lidar profiles through the dust layers. The Falcon flight tracks presented in this study are indicated in Figure 1. Lidars were used to determine optical dust properties, particle shape, and temporal evolution of dust layers, complemented with Sun photometer measurements. To support this campaign, satellite observations such as Meteosat Second Generation (MSG) and Multiangle Imaging Spectroradiometer (MISR) were used to support the ground-based and airborne measurements. Even if dust emissions and depositions were not measured during this campaign, SAMUM-1 creates a deeper understanding of dust properties and of the dust cycle in the Sahara with models as one of the tools aimed at figuring that out. The measurements and observations of the campaign give a unique opportunity to constrain the COSMO-MUSCAT regional model (Consortium for Small-Scale Modeling-Multiscale Chemistry Aerosol Transport, named Lokal Modell-MUSCAT in previous studies). The modeling works performed by *Heinold et al.* [2007, 2009] point out the ability of the COSMO-MUSCAT model to describe dust transport in the mesoscale and the regional dust radiative effect. Nevertheless, these first results indicate that a more complete study of the dust emissions and the size distribution of dust emitted is needed to simulate the Saharan mineral dust cycle.

[5] Therefore the first aim of this study is to understand dust emissions and distributions using the COSMO-MUSCAT model, which we adjust to be as physically based as possible. The recent developments of a specific database of soil properties are used to characterize key erosion parameters such as the surface roughness length, the soil grain size distribution, and the soil texture [*Laurent et al.*, 2008a]. This database is used with the dust module of COSMO-MUSCAT for the Sahara, which is generally considered to be the major source region of mineral dust worldwide [*Prospero et al.*, 2002]. Moreover, we investigate how to represent more realistically the dust size distribution in the model compared with the previous study of *Heinold et al.* [2009]. To do this, our approach is based on wind tunnel measurements performed by *Alfaro et al.* [1998] and the sandblasting model developed by *Alfaro and Gomes* [2001].

[6] Our second aim is to deliver geophysical information about Saharan dust emission, transport, and deposition. The locations of the dust source areas, the daily dust emissions, and their size distribution are computed using the new model developments over the main desert areas of the Sahara (Figure 1). Total emitted dust load and dry and wet deposition of dust are quantified for the SAMUM-1 campaign period. The simulated dust cycle and the current limits of the regional dust modeling are discussed with regard to SAMUM-1 measurements, meteorological stations, and satellite observations. Specific comparisons between modeled emissions, dust source areas backtracked using Meteosat Second Generation dust products, and meteorological station observations are done. The dust size distribution is compared with SAMUM-1 measurements and Aerosol Robotic Network (AERONET) inversion data. This paper also highlights the importance of evaluating the model outputs using the complementary dust products currently available. The input data sets we use and our validation method represent a clear sophistication of the modeling of Saharan dust emissions.

2. Regional Dust Model System COSMO-MUSCAT

[7] The parallelized regional model system COSMO-MUSCAT was developed to describe Saharan dust emission, transport, and deposition, together with the regional

dust radiative effect [*Heinold et al.*, 2007; *Helmert et al.*, 2007; *Heinold et al.*, 2008]. This model system was already used for dust case studies within the framework of the Bodélé Dust Experiment (BoDEx) [*Tegen et al.*, 2006] and the SAMUM-1 campaign [*Heinold et al.*, 2009]. It is composed of the nonhydrostatic meteorological COSMO (Consortium for Small-Scale Modeling, previously named Lokal Modell LM) [*Steppeler et al.*, 2003], which is the operational weather forecast model of the German weather service (Deutscher Wetterdienst), and the online-coupled Multiscale Chemistry Aerosol Transport model (MUSCAT) [*Wolke et al.*, 2004a, 2004b]. *Heinold et al.* [2007] implemented the process-oriented dust emission scheme on the basis of the work of *Marticorena and Bergametti* [1995] and *Marticorena et al.* [1997] in COSMO-MUSCAT. Here the emission fluxes and transport of mineral dust particles are calculated within the MUSCAT model on the basis of meteorological conditions computed by the COSMO model and updated every advection time step. The local wind systems, clouds, precipitation, and mesoscale convection are simulated depending on topography, and the moist convection is parameterized following *Tiedtke* [1989]. The simulated dust outputs and the meteorological fields of COSMO-MUSCAT are extracted every hour with a horizontal resolution of 28 km × 28 km, and for 40 vertical σ-p levels (terrain following) from surface to 200 hPa. A complete model description is given by *Heinold et al.* [2007, 2009]. Hereinafter the main characteristics of the dust emission and deposition model are briefly presented.

2.1. Dust Emission Scheme

[8] Dust emission is an aeolian erosion process occurring at the interface between the atmosphere and the surface when the wind friction velocity, U^*, exceeds a threshold wind friction velocity, U_t^*. The gravity forces of the soil aggregates and the interparticle cohesive forces reinforcing soil grain bonds lead to an optimum grain size for which U_t^* is minimum [*Chepil*, 1945; *Iversen and White*, 1982]. Moreover, the wind momentum is partly consumed by nonerodible elements present on arid and semiarid surfaces [e.g., *Gillette*, 1979; *Gillette and Stockton*, 1989; *Okin and Gillette*, 2001], and is then less efficient to initiate particle motion. This leads to a decrease of the wind shear stress acting on the erodible surface and to an apparent increase of U_t^*. The physical scheme developed by *Marticorena and Bergametti* [1995] describes the drag partition between roughness elements (characterized by the aerodynamic roughness length, Z_0) and erodible surfaces (characterized by the smooth roughness length, z_{0s}) to parameterize U_t^* for "rough" and "smooth" desert surfaces.

[9] When the erosion threshold is exceeded, the saltation of soil aggregates with the optimum size is initiated. The size-resolved horizontal flux of material mobilized by wind (G in g cm^{-1} s^{-1}) is simulated as a function of U^* as follows:

$$G = E\frac{\rho_a}{g}U^{*3}\sum\nolimits_{D_g}\left(1+\frac{U_t^*(D_g,Z_0,z_{0s})}{U^*}\right)\cdot\left(1-\frac{U_t^*(D_g,Z_0,z_{0s})^2}{U^{*2}}\right)S_{rel}(D_g), \quad (1)$$

where E is the fraction of erodible to total surface, ρ_a is the air density, g is the gravitational constant, and $S_{rel}(D_g)$ is the relative surface covered by the soil aggregates of diameter D_g. E can be estimated using a linear function of the logarithm of Z_0, when Z_0 exceeds a threshold value (further details are given by *Laurent et al.* [2008a]). $S_{rel}(D_g)$ is defined using the basal surface of the soil aggregates, which can be computed from their distribution and assuming spherical particles with the same density [see, e.g., *Marticorena and Bergametti*, 1995].

[10] The dust production corresponds to the breaking of the interparticle bonds linking dust particles together or to the surface when the saltating grains hit the surface. On the basis of *Gillette*'s [1979] coupled measurements of horizontal fluxes (G) and vertical fluxes of all dust particles with diameters less than 20 μm (F in g cm^{-2} s^{-1}), *Marticorena and Bergametti* [1995] established an empirical relationship between the ratio F/G (also called the sandblasting efficiency α) and the soil clay content (i.e., the texture of the soil). This parameterization is used in this study to estimate the mass of F, composed by the finest particles in suspension from the saltation layer that are able to be transported. These particles are transported as passive tracers in five independent size classes (or dust bins) with diameter limits at 0.1 μm, 0.3 μm, 0.9 μm, 2.7 μm, 8 μm, and 24 μm. From in situ and airborne measurements during the SAMUM-1 campaign, *Kandler et al.* [2009] noticed that for particles smaller than 0.5 μm diameter, the particle distributions show maxima around 0.08 μm, largely unaffected by variations in meteorological and dust emission conditions. On the other hand, these authors mentioned that the size distribution of transported dust cannot be followed on the aircraft to sizes much beyond 30 μm particle diameter. Even if this size range does not allow us to simulate the large saltating particle mode (~150 μm) which is emitted locally, it is suitable to study dust transport.

2.2. Dust Deposition Parameterizations

[11] The dry deposition of dust is parameterized following *Zhang et al.* [2001]. As described by *Heinold et al.* [2007], turbulent transfer, Brownian diffusion, impaction, interception, gravitational settling, and particle rebound are taken into account depending on dust particle size diameter (D_p) and density (ρ_p) and on relevant meteorological quantities. The dry deposition velocity v_d is expressed as follows:

$$v_d = \frac{1}{R_a + R_s + R_a R_s v_g} + v_g, \quad (2)$$

where the aerodynamic and surface resistances, R_a and R_s, respectively, are defined following *Zhang et al.* [2001], and v_g is the gravitational settling velocity expressed as follows:

$$v_g = \frac{(\rho_p - \rho_a) g D_p^2 C_c}{18\mu}, \quad (3)$$

with μ being the dynamic viscosity of air. C_c is the Cunningham correction factor accounting for the reduced resistance of viscosity (as particle size approaches the mean free path of the air molecules λ):

$$C_c = 1 + \frac{2\lambda}{D_p}\left[1.142 + 0.558\exp\left(-\frac{0.4995 D_p}{\lambda}\right)\right]. \quad (4)$$

[12] In-cloud and subcloud scavenging are both computed for large-scale and convective precipitation. Following *Heinold et al.* [2007], the details of the parameterization are taken from the EMEP MSC-W Eulerian model [*Tsyro and Erdman*, 2000] and applied for each dust bin. The decrease rate of dust concentration (C_{dust}) of the dust bins (j = 1 to 5) for the vertical levels (k = 1 to 40) due to in-cloud scavenging is computed as follows:

$$\frac{\partial C_{dust}(j,k)}{\partial t} = -C_{dust}(j,k)\frac{W_{in}.P_{(k)}}{\Delta z_{(k)}.\rho_w}, \quad (5)$$

where W_{in} is the in-cloud scavenging ratio, P is the precipitation rate, Δ_z is the height of each model layer, and ρ_w is the water density.

[13] The decrease rate of the dust concentration due to subcloud scavenging is computed as follows:

$$\frac{\partial C_{dust}(j,k)}{\partial t} = -C_{dust}(j,k)\frac{A.P_{(k)}.\overline{E}_{(j)}}{V_{dr}}, \quad (6)$$

where V_{dr} is the raindrop fall speed assumed to be 5 m s^{-1}, A = 5.2 m^3 kg^{-1} s^{-1} is an empirical coefficient (assuming the Marshall-Palmer precipitation size distribution), and $\overline{E}$ is the size-dependent collection efficiency of aerosols by raindrops [*Tsyro and Erdman*, 2000].

[14] Regarding the scavenging by convective precipitation, *Balkanski et al.* [1993] adopted a scavenging efficiency of 0.5 in shallow wet convection and of 1 in deep wet convection for aerosol global circulation simulations. According to *Grini et al.* [2005], convective rain removes dust whenever the air rising in a convective tower becomes supersaturated with an efficiency of 1. Thus we consider that convective rain dust is removed with an efficiency of 1 when ground precipitation is observed simultaneously.

3. Input Data Sets to Model Dust Emissions and Distributions

[15] The performance of the model has previously been partly tested for documented periods of Saharan dust transport to Europe in August and October 2001 [*Heinold et al.*, 2007], for a dust outbreak over the Bodélé, which is considered to be one of the Earth's most active dust sources [*Tegen et al.*, 2006], and for SAMUM case studies [*Heinold et al.*, 2009]. However, the representation of the threshold friction velocity often appears problematic for model applications. Previous studies have solved this problem using a tuning factor of 25% [*Prigent et al.*, 2005] or of 34% in the Bodélé [*Tegen et al.*, 2006] to lower the model threshold friction velocity that must be reached to initiate dust emission. *Heinold et al.* [2007, 2009] also reduced the threshold velocity for the whole Sahara by a factor of 0.66 to ensure correct dust production in COSMO-MUSCAT.

[16] We present here a new approach in the dust representation in COSMO-MUSCAT on the basis of recent Saharan soil data sets specifically developed to model aeolian erosion and on local investigations on meteorological phenomena and surface winds such as in the Bodélé. The size distribution of emitted dust is connected to the dust production processes [*Alfaro and Gomes*, 2001]. On the basis of wind tunnel measurements and the sandblasting model of *Alfaro et al.* [1998] and *Alfaro and Gomes* [2001], specific dust size distributions are established considering soil characteristics. This approach should allow a more realistic description of dust emissions and size-resolved processes.

3.1. Input Emission Parameters

[17] To compute relevant dust emission fluxes, the soil and surface properties (soil grain size distribution, soil texture, and surface roughness length) and the meteorological parameters (surface wind speed) have to be correctly specified in the models. In the present study, we do not consider any more areas as preferential sources. The ability of an area to be erodible and to emit dust is controlled by the surface characteristics and the meteorological conditions without any a priori.

3.1.1. Soil Characteristics

[18] As mentioned in section 2.1, two different soil characteristics are accounted for in the dust emission model developed by *Marticorena and Bergametti* [1995]: (1) the soil size distribution representing the size of the in situ erodible grains and aggregates (D_g) encountered in natural conditions, and (2) the soil texture (clay, silt, and sand proportions).

[19] The soil grain size distribution data set used initially in the model runs by *Heinold et al.* [2007, 2009] was derived from the soil texture classification of the Food and Agriculture Organization (FAO, United Nations Educational, Scientific, and Cultural Organization) [*Tegen et al.*, 2002]. The soil size classes corresponded to clay, silt, medium/fine, and coarse sand populations, or mixtures of these populations, and were assumed to be lognormally distributed with mode diameters at 2 μm, 15 μm, 158 μm, and 720 μm. In previous works, *Tegen et al.* [2002] assumed that the surface material consists of silt-sized aggregates with a median diameter of 30 μm in exposed paleolake areas and enclosed topographic depressions used as preferential sources for dust emissions.

[20] This classification is based on soil information obtained by wet sedimentation techniques which break the soil aggregates (ultrasonic pretreatment, dissolution). This leads to relatively high amounts of loose clay particles which generally form aggregates of larger size (>50–100 μm) and are not encountered most of the time in the natural soils [*Bergametti et al.*, 2007]. Moreover, *Laurent et al.* [2006] pointed out that for northeastern Asian deserts, there is no direct relation between the soil grain size distribution and the soil texture.

[21] In the present study, an alternative approach is chosen following *Marticorena et al.* [1997] and *Laurent et al.* [2008a]. The soil-grain size distribution is obtained using dry techniques that minimize as much as possible the breaking of the aggregates. This approach was used by *Chatenet et al.* [1996] for the characterization of Saharan and Sahelian soils and applied to Chinese desert soil samples by *Mei et al.* [2004]. For the Sahara, *Chatenet et al.* [1996] showed that the dry size distribution of any soil can be determined as a mixture of a maximum of four populations lognormally distributed: alumino-silicated silt, fine sand, coarse sand, and salts, with mode diameters of 125 μm, 210 μm, 690 μm, and 520 μm, respectively. To describe the desert soils of North Africa, *Marticorena et al.* [1997] and *Callot et al.* [2000] defined 12 soil types, each soil type being a mixture of

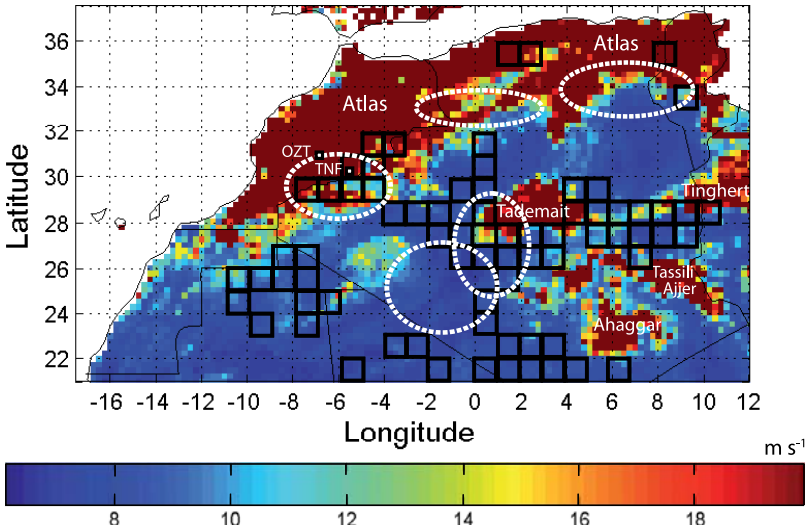

Figure 2. Map of the 10 m erosion threshold wind velocities (28 km × 28 km spatial resolution) over northwestern Africa including the SAMUM-1 area (main SAMUM-1 sites: Ouarzazate (OZT) and Tinfou (TNF), located 30 km southeast of Zagora). The white dotted areas correspond to the estimated source regions of the various dust episodes encountered during the SAMUM-1 research flights [*Petzold et al.*, 2009]. The black squares correspond to the location of the dust emissions observed during the SAMUM-1 period using MSG observations and following the dust backtracking method by *Schepanski et al.* [2007].

the four populations identified by *Chatenet et al.* [1996]. The dry soil size distribution database developed by *Marticorena et al.* [1997] and *Callot et al.* [2000] to model wind erosion processes was updated at the ¼° × ¼° spatial resolution [*Laurent et al.*, 2008a]. Up to two of the different soil types can be attributed to each grid cell to represent small surface units such as the silty or salty depressions [*Laurent et al.*, 2008a]. This updated database of the soil characteristics is now used to simulate dust emissions with COSMO-MUSCAT.

[22] Using *Marticorena and Bergametti* 's [1995] model, the clay content of the soil reported in the soil texture data set is needed to compute the sandblasting efficiency (α), and then the vertical flux of emitted dust. The soil database used in COSMO-MUSCAT by *Heinold et al.* [2007, 2009] led to α values ranging from 10^{-5} cm^{-1} to 10^{-7} cm^{-1} for silt, fine/medium sand, and coarse sand, respectively [*Tegen et al.*, 2002]. The highest α of 10^{-5} cm^{-1} was used for the preferential source areas located in topographic depressions for the *Heinold et al.* [2007, 2009] runs of the model.

[23] Here again, we use an updated data set of α values computed from various North African soil textures by *Laurent et al.* [2008a] without any a priori assumption of whether areas are preferential sources. The sandblasting efficiency is then directly connected to the soil characteristics and ranges from 10^{-6} cm^{-1} for the coarse sand to about 2×10^{-5} cm^{-1} for the agricultural soil. This range is consistent with the measurements performed by *Gillette* [1979] and the estimations for the soils of northeastern Asian deserts made by *Laurent et al.* [2006].

3.1.2. Surface Roughness Length

[24] Surface roughness length (Z_0) is a key parameter to compute dust emissions. *Marticorena et al.* [2004] investigated the possibility of retrieving Z_0 of arid areas using surface products derived from passive multidirectional measurements of the Polarization and Directionality of the Earth Reflectance (POLDER-1) spaceborne sensor. An empirical relationship between Z_0 and a protrusion coefficient (*PC*) derived from the POLDER-1 bidirectional reflectance distribution function (BRDF) was established [*Marticorena et al.*, 2004]. Such a Z_0 data set was already used in COSMO-MUSCAT by *Heinold et al.* [2007]. Owing to the selection on the quality and the consistency of the satellite data and to persistent cloud cover, data were missing in particular in the south of Mauritania and Mali, the Bilma Erg, and a part of the Bodélé. For these areas, *Laurent et al.* [2008a] estimated Z_0 values considering the neighboring pixel values, Z_0 estimated from a geomorphologic analysis of North African landscapes [*Marticorena et al.*, 1997; *Callot et al.*, 2000], and local to regional geomorphologic and topographic context. The updated composite map of Z_0 established by *Laurent et al.* [2008a] is now used to compute threshold wind friction velocities.

[25] We compute the 10 m threshold wind velocities from the threshold wind friction velocities computed by *Laurent et al.* [2008a] assuming a neutral logarithmic wind profile. The values reported in Figure 2 indicate the range of 10 m wind speeds needed to exceed erosion thresholds for the SAMUM-1 study area in northwestern Africa. The two ground stations where the SAMUM-1 experiment was concentrated, Ouarzazate and Tinfou, are also presented in Figure 2. High roughness lengths in mountainous terrain, such as in the Atlas or in the Ahaggar, lead to high threshold wind velocities (higher than 18 m s^{-1}) and should make dust emission difficult or impossible. Flat and smooth terrains with threshold wind velocities below 10 m s^{-1} provide more favorable conditions for dust emission, depending on the granulometry of soil aggregates. Areas presented as dust sources for the major dust events during SAMUM-1 by backward trajectory studies by *Petzold et al.* [2009] are outlined with white

Table 1. Median Mass Diameter and Geometric Standard Deviation for the Three Aerosol Particle Populations That Can Be Released From Arid Soils[a]

	Dust Mode 1	Dust Mode 2	Dust Mode 3
Median mass diameter, d_n (μm)	1.5	6.7	14.2
Standard deviation, σ_n	1.7	1.6	1.5

[a]From *Alfaro and Gomes* [2001].

dashed lines. With its high spatiotemporal resolution, the MSG SEVIRI (Spinning Enhanced Visible and Infrared Imager) infrared dust index allows us to discern the origin of major dust emission events in a qualitative way [*Schepanski et al.*, 2007]. For the SAMUM-1 period, the 1° × 1° grid cells where dust source activations are observed by MSG SEVIRI are also outlined in Figure 2 as black squares. These results suggest that dust emissions can occur both in smooth terrains for low to medium threshold wind velocities and in the vicinity of mountainsides when strong surface winds occur. Comparing the results in Figure 2 to the landform map from *Ballantine et al.* [2005], we can conclude that dust can be emitted from various surface types (e.g., regs, alluvial, dunes), but only when the erosion thresholds are exceeded.

3.1.3. Surface Meteorological Parameters

[26] The COSMO meteorological model driven by the global model of DWD (GME) meteorological fields is used to simulate regional dust emission, advection, and transport for most of the Saharan desert areas. Even if the model simulated most of the meteorological fields well, some surface dynamics are sometimes not well represented in the model owing to specific atmospheric conditions, topographic situations, or surface characteristics [*Laurent et al.*, 2008b]. Our approach is thus to improve the representation of the surface meteorological fields for well-known critical regions. This is done only when we have relevant geophysical information to do such a correction. Following the BoDEx campaign, several studies showed that the Bodélé emissions could be underestimated owing to low model surface wind speeds [*Bouet et al.*, 2007; *Laurent et al.*, 2008b; *Todd et al.*, 2008a]. In this area, the low-level jet, which may play an important role for dust mobilization, seems to be well reproduced by the COSMO-MUSCAT model [*Schepanski et al.*, 2009a]. Moreover, the COSMO-MUSCAT 10 m wind speeds reproduce correctly the daily cycle and the peak winds of 3 m wind speed measured in the Bodélé during the BoDEx campaign [*Laurent et al.*, 2008b]. Assuming a neutral logarithmic wind profile, the assessment of the 3 m measured wind speeds for a 10 m height are nevertheless 10% higher than the simulated 10 m wind speeds. This underestimation can be due to the representation of the planetary boundary layer (PBL) in the model. In fact, the PBL processes link the LLJ breakdown and surface winds. As mentioned by *Todd et al.* [2008b], a key requirement of the models in the Bodélé is the relevant simulation of the intensity and phase correlation of LLJ and surface winds. To compensate for this underestimation, the surface wind speed is increased by 10% for a delimited Bodélé area roughly extending from 16°N to 18°N and from 16.5°E to 19°E. Such a correction of the wind speed in the Bodélé is possible thanks to the in situ measurements of the BoDEx experiment. Other specific areas of the Sahara should deserve the same approach, but unfortunately the lack of in situ measurements does not allow us to better describe the surface-atmosphere interactions for these areas at the present time.

[27] Soil moisture does not noticeably affect the Saharan dust emissions and their interannual variability, but it can partly control and limit dust emissions in some parts of the northern desert margin, where the precipitation rates are higher [*Laurent et al.*, 2008a]. Moreover, *Belnap et al.* [2004] mentioned that soil surfaces can dry quickly, for instance, in desert areas of the United States. Monitoring of soil under field conditions showed that owing to high air temperatures, precipitation events less than 3 mm often resulted in soils being wet for less than 30 min [*Belnap et al.*, 2004]. We consider that surface precipitation in a grid cell during a time step inhibits dust emission but does not produce any lasting soil moisture effect beyond this time step. Not considering the water retention by the soil and the soil crusting after a rainfall event, dust emissions may be overestimated after an intense rainfall event. This simplified approach based on the occurrence of surface rainfall allows us to roughly consider the short-term limitation of surface rainfall on dust emissions.

[28] To conclude this section on dust emission parameters, it should be noted that the issue of surface dynamics (e.g., temporary surface crusts, seasonal vegetation, and supply limitation) is still largely unresolved in the modeling community. Here, for instance, we are not able to parameterize temporal changes in soil crusts. The COSMO-MUSCAT model uses the BIOME4 global data set, which gives a rough, static description of land use and does not allow for the investigation of the dynamic aspects of vegetation. In situ observations suggest that horizontal flux can be strongly dependent on vegetation distribution [*Okin and Gillette*, 2001]. In the arid areas of the Sahara, the cultivated lands and partly vegetated areas have very sparse vegetation cover, except in some areas in the northern margins of the studied areas. From observation in the Chihuahuan desert, United States, *Okin and Gillette* [2001] found that vegetation close to the threshold at which it drops dust emission can actually enhance emissions by exposing elongated areas of bare soil, or "streets," to strong winds. More recently, *Okin* [2005] pointed out the importance of landscape heterogeneity in dust emission and the need to quantify heterogeneity at multiple scales in sparsely vegetated landscapes. Here we roughly consider that the contribution of these surfaces to the Saharan dust budget should stay limited. A better characterization of the dynamics of the surface would require complementary investigation using dynamic vegetation model, land use cartography, and satellite information. Therefore we assume that the potential for dust emission from the surface is constant in time.

3.2. Representation of the Dust Size Distribution

[29] The representation of the model dust size distribution is also a key point to simulate correctly the size-dependent process, like the deposition, and to quantify the dust aerosol optical thickness. Until now, the dust size distribution simulated by COSMO-MUSCAT reflected the original soil size spectrum described by the soil populations [*Heinold et al.*, 2007, 2009]. For the dust emitted from the preferential sources, *Heinold et al.* [2009] considered that during the

Table 2. Mass Proportion of the Three Particle Modes of Released Dust for the Main Soils of North Africa for U^* = 55 cm/s[a]

Soil	Dust Mode 1	Dust Mode 2	Dust Mode 3
Silty fine sand (SFS)	4	29	67
Medium sand (MS)	48	28	24
Coarse sand (CS)	59	27	14
Coarse medium sand (CMS)	54	27	19
Fine sand (FS)	5	30	65
Silty medium sand (SMS)	21	28	51
Moderately salty silt (SEM)	30	32	38
Highly salty silt (SEF)	33	33	34

[a]Values are given in percent and are computed using the mode proportions of four arid soil components as described by *Alfaro and Gomes* [2001].

saltation, the particles degraded into smaller dust particles with a mode diameter of 2 μm and a standard deviation of 2. The originally emitted dust particles were then assigned in the five dust bins.

[30] In the present study, we follow an approach different from that of *Heinold et al.* [2009]. To simulate the initial size distribution of emitted dust particles, the sandblasting process has to be taken into account. The soil grains in saltation provide the kinetic energy to produce transported fine dust from the breaking of the cohesive forces linking fine particles to soil aggregates. Two physical models describing the sandblasting process have been developed by *Alfaro and Gomes* [2001] and *Shao* [2001]. *Alfaro and Gomes* [2001] combined their sandblasting model with the saltation model of *Marticorena and Bergametti* [1995].

[31] On the basis of wind tunnel observations, *Alfaro et al.* [1998] and *Alfaro and Gomes* [2001] showed that the dust mass particle size distribution of produced dust is a mixture of three particle populations. These three populations, which can be released from arid soils, can be represented by three lognormal modes defined by specific mass median diameter (d_n) and geometric standard deviation (σ_n) (Table 1). Only the relative proportion of the three modes varies as a function of the balance between the kinetic energy of the soil grains in saltation (e_c) and the binding energy (e_n) of the three particle populations. *Alfaro and Gomes* [2001] expressed e_c of assumed spherical soil aggregates (characterized by its density ρ_p, and its granulometry D_g) as a function of the wind friction velocity:

$$e_c = \rho_p \frac{\pi}{12} (D_g)^3 \left(20U^*\right)^2. \quad (7)$$

[32] The numerical values of e_n were estimated on the basis of wind tunnel measurements [*Alfaro et al.*, 1998; *Alfaro and Gomes*, 2001]: e_1 = 3.61 g cm^2 s^{-2}, e_2 = 3.52 g cm^2 s^{-2}, and e_3 = 3.46 g cm^2 s^{-2}. However, *Alfaro* [2007] mentioned that if soil texture and composition have no effect on e_n, it does not mean that they do not have an indirect effect on a soil's overall susceptibility to wind erosion. *Gomes et al.* [2003] and *Alfaro et al.* [2004] used e_n reduced by a factor 3 for a soil from Niger. The recent works of *Sow et al.* [2009] pointed out the necessity to perform new coupled studies (in situ measurements, wind tunnel measurements, and model development) to validate or, if necessary improve, the model. For the Bodélé, which is a distinctive source because of its large exposure of diatomite and the presence of megabarchan dunes [*Chappell et al.*, 2008], *Warren et al.* [2007] mentioned that the diatomite soil flakes in the Bodélé have much lower binding strengths than quartz sand or soil aggregates. *Tegen et al.* [2006] assumed e_n reduced by a factor 20 to break up the saltating diatomite particles compared with the results derived for breakup of clay aggregates by *Alfaro et al.* [1997].

[33] These corrective factors applied to the binding energies point out the current model limits to determine which U^* is needed for a saltating soil aggregate of diameter D_g to provide enough kinetic energy to produce fine dust. Moreover, *Sow et al.* [2009] analyzed two events of the monsoon type and one of the convective type in detail. They showed that the size distribution of the dust released by a given event is fairly constant and insensitive to even relatively important variations of U^*. The authors interpreted this result as a possible consequence of the rather long duration (15 min) over which wind fluctuations must be averaged for computing U^*. During these events, U^* ranges from 30 cm s^{-1} to 60 cm s^{-1} for the monsoon events and from 40 cm s^{-1} to 80 cm s^{-1} for the convective event [*Sow et al.*, 2009]. In such conditions, we choose a simplified approach to determine the relative proportions of the three dust modes. On the basis of the work by *Alfaro and Gomes* [2001], a typical dust particle size distribution is determined for each soil type under a medium wind friction velocity U^* of 55 cm s^{-1} (Table 2). *Foret et al.* [2006] indicated that such a value of U^* is a compromise between the high values observed during strong events for high but infrequent wind speeds and those observed during most frequent dust events occurring for wind speeds just above the erosion threshold.

[34] Moreover, *Todd et al.* [2007] indicated a dominant dust mode with a diameter centered between 2 and 4 μm in the Bodélé, the shape of the particle size distribution being similar in relatively clear and dusty conditions. To be consistent with these in situ observations for this specific area, we attribute the dust mass distribution which produces the finest particles (59%, 27%, and 14% of the dust mass distributed in the modes centered on particle diameters of 1.5, 6.7, and 14.2 μm, respectively) to the dust emitted in the Bodélé area (extending from 16°N to 18°N and from 16°E to 19.5°E).

[35] The transported dust mass (M_n) of each of the three modes is assumed to be lognormally distributed. It is redistributed in the five model dust bins (M_i) (diameter limits *di*: 0.1 μm, 0.3 μm, 0.9 μm, 2.7 μm, 8 μm, and 24 μm) using the following mass repartition scheme [*Schulz et al.*, 1998; *Zender et al.*, 2003]:

$$M_i = \sum_n \frac{M_n}{2} \left[erf\left(\frac{\ln\left(d_{i,\max}/d_n\right)}{\sqrt{2}\ln\sigma_n}\right) - erf\left(\frac{\ln\left(d_{i,\min}/d_n\right)}{\sqrt{2}\ln\sigma_n}\right)\right], \quad (8)$$

where *erf* is the standard error function, $d_{i,\min}$ and $d_{i,\max}$ are the minimum and maximum diameters of bin i, and d_n and σ_n are the mass median diameter and geometric standard deviation of the source dust modes reported in Table 1.

[36] The new developments in the dust emission representation in COSMO-MUSCAT presented in this section com-

Table 3. Dust Emission Model Details

	Dust Emission [*Heinold et al.*, 2009]	Dust Emission (This Study)
Emission scheme	following *Marticorena and Bergametti* [1995]; erosion threshold computed with a 0.66 corrective factor	following *Marticorena and Bergametti* [1995]
Surface winds	computed by COSMO	computed by COSMO; specific correction for the Bodélé regarding comparison between model and in situ measurements
Surface roughness	derived from POLDER 1 satellite products [*Marticorena et al.*, 2004]	updated data derived from POLDER 1 satellite products and geomorphologic information [*Laurent et al.*, 2008a]
Soil texture (clay, silt, sand)	based on *Zobler* [1986], except in preferential source regions where uniform texture is applied [*Tegen et al.*, 2002]	estimated from soil samples and geomorphologic analysis of desert regions [*Laurent et al.*, 2008a]
Soil grain size distribution	derived from the soil texture data [*Tegen et al.*, 2002]	established from soil samples and geomorphologic analysis of desert regions [*Laurent et al.*, 2008a]
Land use data	27 potential vegetation types from equilibrium terrestrial biogeography model BIOME4 of *Kaplan* [2001]	27 potential vegetation types from equilibrium terrestrial biogeography model BIOME4 of *Kaplan* [2001]
Sandblasting efficiency	estimated for each soil type and ranging from 10^{-7} to 10^{-5} cm^{-1} [*Tegen et al.*, 2002]	computed for each soil type and ranging from 10^{-6} to 2 10^{-5} cm^{-1} [*Laurent et al.*, 2008a]
Dust size distribution	derived from *Tegen et al.* [2002]	derived from *Alfaro and Gomes* [2001]; specific dust size distribution used for the Bodélé regarding in situ observations
Dust bins	five size bins for dust transport with lognormal distribution for the range 0.2–48 μm in diameter	five size bins for dust transport with lognormal distribution for the range 0.1–24 μm in diameter

pared to the study of *Heinold et al.* [2009] are summarized in Table 3.

4. Mineral Dust Emissions and Distributions During SAMUM 2006

[37] In this section, the results of the dust simulation using the new model developments are discussed. As a first step, the dust emission source areas, the dust load quantification, and the occurrences of dust emissions are investigated for the SAMUM-1 period. Simulations are performed for the period 10 May to 5 June 2006. Next, mineral dust distributions, main transport, and deposition patterns are discussed for SAMUM-1 dust events.

4.1. Source Areas, Dust Load Quantification, and Occurrences of Dust Emissions

[38] The location of the source areas is presented on the map of the total dust emissions for the SAMUM-1 period (Figure 3). The dust emission simulations using the new model developments (Figure 3b) are compared with results from the previous study of *Heinold et al.* [2009] (Figure 3a) for the same area and the same period. It can be noticed that the locations of the main source areas remain quite similar for the two studies, as, for example, the Bodélé and the north of Algeria. In the latter area, the two simulated intense dust events of 24–26 May and 31 May to 1 June mainly cause high dust loads. *Knippertz et al.* [2007, 2009] described how during 24–26 May a cutoff low that formed over northwestern Africa was associated with unsettled

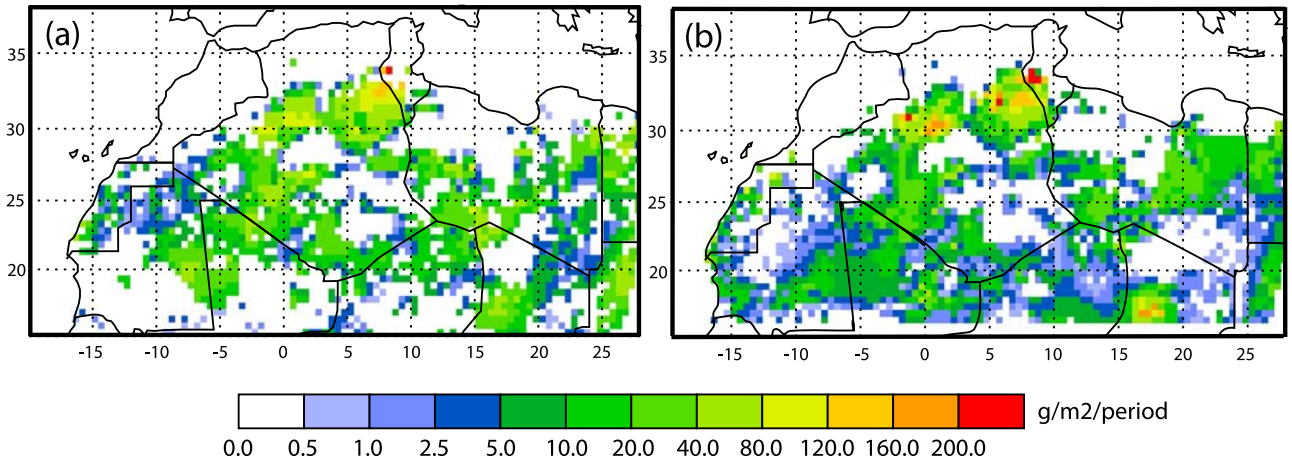

Figure 3. Maps of the total dust emission for the studied area between 10 May and 5 June 2006: model results by (a) *Heinold et al.* [2009] and (b) this study.

weather conditions in the entire region and caused strong surface winds up to 15 m s^{-1}, blowing sand and precipitation in the vicinity of the Anti-Atlas and the Moroccan and Algerian border. For the severe dust event of 31 May to 1 June, *Knippertz et al.* [2009] concluded that the main dust sources appear to be located in northeastern and central Algeria and close to Tunisia. Dust mobilization was associated with a cold surge from the Mediterranean and wind speeds of more than 20 m s^{-1} at 925 hPa [*Knippertz et al.*, 2009]. However, the relative intensities of several source areas, such as the southwest of Algeria, the Mauritania-Mali border, and southwestern and northeastern Libya, differ from one study to the other. For instance, the simulations of *Heinold et al.* [2009] resulted in more intense emissions from the area between Mauritania and Mali than in ours. Some discrepancies can also be noticed with regard to the location of less intense sources. Using the new model developments, emissions are now simulated over an extended area in Mauritania and Mali, in the south of Niger, and in middle Libya.

[39] The Saharan dust emissions simulated for the SAMUM-1 period (10 May to 5 June) are 88 Tg in the work by *Heinold et al.* [2009] and 78 Tg in this study. A difference of more than 10% is observed regarding the total dust load emitted by these two model versions. Both results are in the range of those of previous studies. Investigating dust load for 1981 and 1982, *D'Almeida* [1986] estimated the dust load emitted from the Sahara to be 67.6 for May 1981 and May 1982 and 86.2 Tg for June 1981 and 92.6 for June 1982. Moreover, *Laurent et al.* [2008a] simulated Saharan dust emissions for 6 years from 1996 to 2001 and obtained mean dust emissions of 78 ± 21 Tg for May and 73 ± 20 Tg for June. The annual dust emissions proposed by *D'Almeida* [1986] and *Laurent et al.* [2008a] for the Sahara range from 630 to 710 Tg yr^{-1} and from 585 to 760 Tg yr^{-1}, respectively. The annual Saharan dust load ranges generally from 240 Tg yr^{-1} using satellite observations [*Kaufman et al.*, 2005] to 760 Tg yr^{-1} [*Callot et al.*, 2000] and 1430 Tg yr^{-1} [*Ginoux et al.*, 2004] using modeling approaches (a data compilation of the estimates of mean annual dust emissions for North Africa is given by *Engelstaedter et al.* [2006]). At the present time, there is no unquestionable quantitative observation of the dust emissions over the Sahara. However, indirect observations of emitted and transported dust can be used to test whether the simulations are reasonable, at least in terms of spatial and temporal variations.

[40] The spatial and temporal variability of the simulated dust emissions and source areas is evaluated with regard to satellite and meteorological station observations. The occurrences of "significant" dust emissions (corresponding to dust flux > 10^{-10} g cm^{-2} s^{-1}) and more "intense" emissions (dust flux > 10^{-9} g cm^{-2} s^{-1}) are simulated with a 28 km × 28 km resolution (Figure 4, first and second columns, respectively) for five dust and intermediate phases (DPs and IPs) of the SAMUM-1 campaign in 2006 as defined by *Knippertz et al.* [2009]: DP1 (13–15 May), IP1 (16–21 May), DP2 (22–27 May, except 25 and 26 May for which MSG data are not available), IP2 (28–30 May), and DP3 (31 May to 5 June). Following *Schepanski et al.* [2007], dust emission occurrences observed from MSG SEVIRI IR difference images are established using a backtracking approach for the same five periods (Figure 4, third column). Only the first pixel (1° × 1°) where dust is emitted is taken into account and reported on the maps. In Figure 4, the results are presented in frequency, i.e., the proportion of days for which a dust event is observed during each period. The arrows show the main directions of the dust plumes under which emitted and transported dust cannot be differentiated. Moreover, the occurrences of dust observed by 12 World Meteorological Organization (WMO) stations (visibility <5 km due to dust) are computed for the five periods (Figure 4, fourth column). The horizontal visibilities less than 5 km measured by the meteorological stations of North Africa allow the determination of the general trend of the dust variability [*N'Tchayi et al.*, 1994; *N'Tchayi et al.*, 1997; *Mahowald et al.*, 2007]. *Mahowald et al.* [2007] evaluated several different visibility proxies at the AERONET sites and chose to use the 5 km threshold on the visibility (a complete description of their method is given by *Mahowald et al.* [2007]). We ensure that this information is due to dust taking into account only the cases for which dust observations (dust raised by wind, dust devil, and dust storm) are reported at the same time as the observations of visibilities less than 5 km. The comparison between the "significant" and "intense" dust emission occurrences (Figure 4, columns 1 and 2, respectively) allow us to locate the places where frequent but less intense emissions take place. These areas are, for instance, the western Saharan coast and Mauritania. More intense emissions are simulated in the Bodélé, in northern and eastern Mali, and in western and western Algeria, depending on the period. The MSG observations (Figure 4, column 3) may correspond to more intense dust emissions. Here we consider only the first location where dust emission is reported (with no cloud or dust stagnation). Then this information can be considered as a minimum dust occurrence.

[41] In general, the spatiotemporal variability of dust source areas shown by the MSG dust products and the dust observations at meteorological stations is well captured by the model for the simulated intense dust emissions. For the DP1 period, the simulations and observations both point out, the south of Algeria and the Bodélé as source areas, and the middle east and west of Algeria with a light shift. For the IP1 period, a close agreement is observed for the dust observations and simulations in the Bodélé, the east of Mali, southwestern Algeria, and south of Mauritania. But simulated emissions occur in eastern Mauritania, whereas emission is not observed with MSG. For the DP2 and IP2 periods, the simulated intense emissions correspond to observations in the Bodélé, the north of Niger, and the east of Mali. Our emissions seem to be overestimated in central and eastern Algeria with regard to MSG observations. These areas are downwind dust sources located on the border between Morocco and Algeria, in southern Algeria and eastern Mali, and therefore cannot easily be detected using our backtracking method. But for these two periods, the simulations capture the frequency fluctuations of dust raised by wind and dust storm observed by the meteorological stations over these areas (i.e., frequencies higher than 75% for DP2 and higher than 60% for IP2). For DP2 and IP2, the simulated emissions are too frequent when compared with observations in east Mauritania and at the border between Mauritania and Mali, respectively. Finally, for the DP3 period, close matches between simulations and observations are observed for the source areas located in Mauritania,

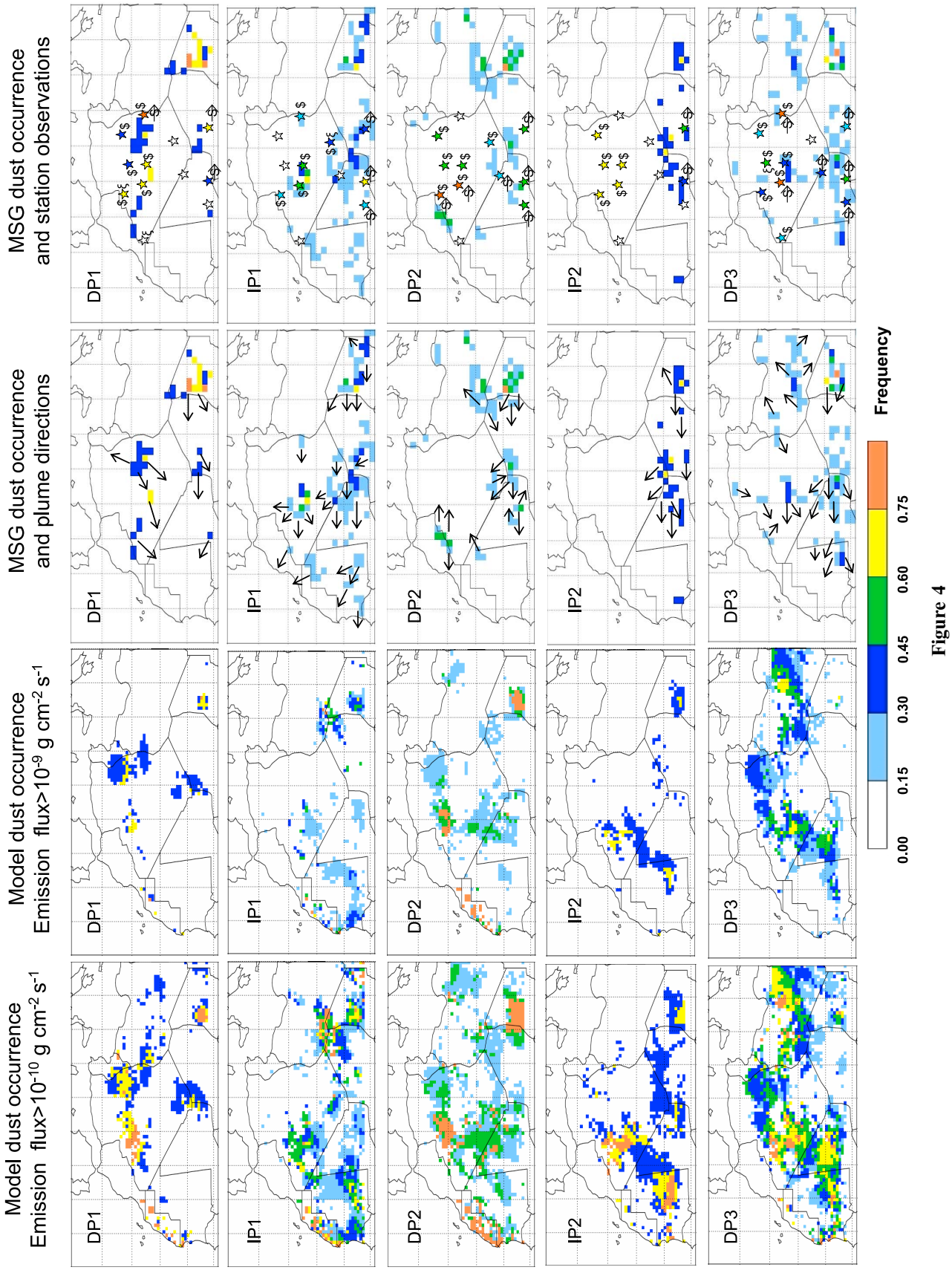
Model dust occurrence
Emission flux>10-10 g cm-2 s-1
Model dust occurrence
Emission flux>10-9 g cm-2 s-1
MSG dust occurrence
and plume directions
MSG dust occurrence
and station observations
DP1
IP1
DP2
IP2
DP3
0.00
0.15
0.30
0.45
0.60
0.75
Frequency

Figure 4

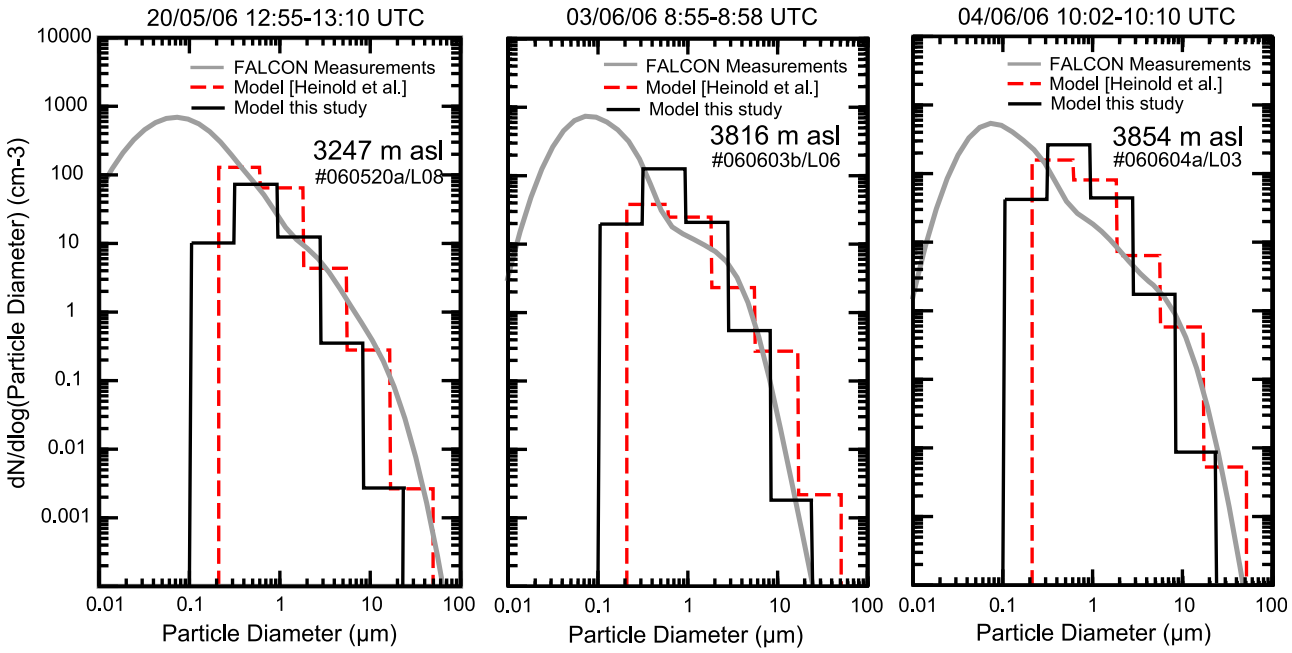

Figure 5. Number size distribution above Ouarzazate (30.9°N, 6.9°W) on (left) 20 May 2006, (middle) 3 June 2006 and (right) 4 June 2006. Particle size distribution from airborne measurements aboard Falcon aircraft [*Weinzierl et al.*, 2009] (gray line), model results from *Heinold et al.* [2009] (red dotted line), and this study (black line).

Mali, and the Bodélé. An overestimation of the simulations can be noticed in Libya, where no station observations are available. Here again, the discrepancies can be partly explained by the fact that MSG cannot observe new dust emissions downwind from previous sources of dust emissions and dust plumes. For this period, the simulated intense emissions seem to be overestimated in Algeria compared with MSG observations but correspond to the surface observations reported by the stations. On the basis of meteorological and surface information, *Knippertz et al.* [2009] mentioned that important dust sources appear to be located in northeastern and central Algeria and close to Tunisia during the 31 May to 1 June period, which corresponds to our simulations.

[42] This evaluation work of dust emission variability and source location points out the necessity to compare simulated emissions with different available data sets. Satellite and surface station observations give complementary information to document local to large-scale dust events. This conclusion is reinforced by the fact that the downwind obscuring effect of the plume in the MSG data can once again be partly responsible for the model-satellite discrepancies.

4.2. Modeled Mineral Dust Distribution, Transport, and Deposition

[43] The patterns of dust transport and deposition are mainly controlled by the dust size distribution and meteorological conditions. To simulate the middle- and long-range transport of dust events correctly, we discuss the model representation of the dust size distribution as well as the vertical and horizontal distributions of dust for case studies of documented Saharan dust events.

4.2.1. Model Size Distribution of Transported Dust

[44] The new representation of the dust size distribution is evaluated with regard to previous model study results and SAMUM-1 measurements. Following *Heinold et al.* [2009], comparisons between number size distributions simulated and the SAMUM-1 airborne measurements aboard Falcon aircraft of the German Aerospace Center (Deutsches Zentrum für Luft- und Raumfahrt, DLR) [*Weinzierl et al.*, 2009] are presented in Figure 5 for 20 May, 3 June, and 4 June 2006 over the location of Ouarzazate, which was one of the SAMUM-1 ground-based stations. A correct description of the dust size distribution is a prerequisite to model size-dependent processes such as the deposition, and size-

Figure 4. Maps of dust emissions for five periods of the SAMUM-1 campaign (DP1, 13–15 May; IP1, 16–21 May; DP2, 22–27 May, except the 25 and 26 for which MSG data are not available; IP2, 28–30 May; DP3, 31 May to 5 June). First and second columns show occurrences of simulated "significant" emissions (dust flux > 10^{-10} g cm^{-2} s^{-1}) and "intense" emissions (dust flux > 10^{-9} g cm^{-2} s^{-1}). Third column shows dust emission occurrences observed from MSG SEVIRI IR difference images using a backtracking approach; the arrows show the main directions of dust plumes under which emitted and transported dust cannot be differentiated. Fourth column shows occurrences of dust observed by 12 WMO stations (visibility < 5 km due to dust raised by wind (dollar sign), dust devil (zeta), and dust storm (arrowed S). The stations are represented by star symbols colored according to the frequency color bar.

dependent parameters, as, for instance, the aerosol optical thickness.

[45] On 20 May, the coarse particle modes (with diameter > 2.7 μm) simulated in this study were lower than previous model results of *Heinold et al.* [2009]. In fact, we clearly underestimated the number of larger particles, but the number of particles <2.7 μm corresponds to the Falcon measurements. On 3 June, the new simulations better catch the measured size distribution for the entire studied spectrum, when the previous simulations of *Heinold et al.* [2009] overestimated the number of particles >2.7 μm. On 4 June, similar distributions are computed by the two studies; the simulations tally with the measurements in both cases. The measured high number of particles <0.5 μm diameter is most likely not related to dust concentrations. As mentioned previously, *Kandler et al.* [2009] noticed that for these small particles, the dust distributions show maxima around 0.08 μm, largely unaffected by variations in meteorological and dust emission conditions that were observed during the SAMUM-1 campaign. *Weinzierl et al.* [2009] suggested that particles smaller than 0.5 μm have a nonvolatile core with a volatile coating. However, the simulated size spectrum of dust particles well matches the measurements performed in the troposphere for 20 May, 3 June, and 4 June. These comparisons seem to indicate that as with the study performed by *Heinold et al.* [2009], the simulated dust layers for these days at Ouarzazate are reproduced correctly both in location and in intensity.

[46] To go further in the size distribution evaluation, comparisons between the volume size distribution simulated and columnar averaged size distributions derived from AERONET spectral aerosol optical depth inversion products (Version 2) [*Dubovik et al.*, 2006] are presented for four different sites: Ouarzazate located in the SAMUM-1 area (30.9°N, 6.9°W), Lampedusa located in the Mediterranean Sea (35.5°N, 12.6°E), Agoufou located at the limit between southern Sahara and Sahel (15.35°N, 1.5°W), and Tamanrasset located in middle Algeria (22.8°N, 5.5°E) (Figure 6). The columnar distribution constant in height is computed as it was for the AERONET distribution. Results are shown for 3 days of the studied period (18 May, 29 May, and 4 June) for which observations are available for the four stations.

[47] As mentioned previously for the comparison with SAMUM-1 measurements, the dust model system is not able to reproduce the submicron particle mode (below 0.5 μm diameter or 0.25 μm radius as presented in Figure 6). It may be that this mode is not principally affected by mineral dust. On the basis of the study by *Dubovik et al.* [2006], *Schepanski et al.* [2009b] mentioned that the observed maximum of the volume size distribution in the fine mode size range (around 0.1 μm in radius) may be an artefact due to the inversion algorithm. Considering the coarser particle range, the model dust particle volume size distributions correspond to the measurements. The relative intensity and the temporal variability of the dust size distribution due to dust transported from different sources are generally well matched for the four stations. For instance, the results between Agoufou and Lampedusa always differ by 1–2 orders of magnitude. This is observed for the measurements as well as for the simulations. However, the model underestimates the intensity of the coarse mode at Lampedusa site for dust transported over the Mediterranean Sea. The close match for the four sites and several days supports the fact that the model dust size distribution is realistically simulated.

4.2.2. Horizontal and Vertical Dust Distribution for SAMUM-1 Case Studies

[48] For the studied days (18 May, 29 May, and 4 June) the dust horizontal distribution is also investigated comparing the model-derived aerosol optical thickness (AOT) with the satellite observations, the Aqua-MODIS Deep Blue AOT, and the Ozone Monitoring Instrument (OMI) semiquantitative Aerosol Index, and AERONET AOT measurements (Figure 7).

[49] MODIS's Deep Blue AOT product [*Hsu et al.*, 2004] uses narrowband measurements at the deep-blue part of the visible part of the spectrum (0.412 μm, 0.47 μm, and 0.65 μm for MODIS) and provides qualitative information on total aerosol column load using lookup tables. In contrast to AOT products at visible wavelength, the Deep Blue product is able to detect airborne aerosol over bright surfaces such as the Saharan desert. In this work, the Aqua MODIS Deep Blue AOT global 1° × 1° data set MYD008_D3.051 is used for comparison.

[50] Originally developed for Total Ozone Mapping Spectrometer (TOMS) measurements by *Herman et al.* [1997], the OMI aerosol index is based on measurements taken at the UV part of the spectrum (0.34 μm and 0.38 μm). Owing to low surface reflectivity at this wavelength [*Eck et al.*, 1987] and spectrally varying absorption characteristics of aerosol particles such as dust and soot, an index sensitive for UV-absorbing aerosols is designed. The algorithm is able to detect aerosol particles over both dark and bright surfaces and gives a measure for the atmospheric aerosol content, but there is a sensitivity toward the height of the aerosol layer [*Torres et al.*, 1998]. Thus the age of an observed dust layer might affect the retrieved AI value. Here the OMTO3G.003 (OMAERUV) data set binned on a 1° × 1° global resolution is used. Both retrievals are on a daily noontime basis as Aqua MODIS crosses the equator at 1:30 P.M. local time (LT) and Aura OMI at 1:45 P.M. LT.

[51] Besides Deep Blue AOT and AI, the qualitative MSG IR dust index is used to compare the shape of simulated dust plumes (Figure 7). The dust index is based on brightness temperatures converted radiances measured at 8.7 μm, 10.8 μm, and 12.0 μm wave length (see, e.g., *Schepanski et al.* [2007] for further description). To identify airborne dust, the split-window technique based on different spectral variability of dust particles at these wavelengths is applied [*Ackerman*, 1997]. The MSG satellite is located geostationary over the Gulf of Guinea and provides measurements every 15 min.

[52] Following *Helmert et al.* [2007], the model-derived AOT at 550 nm wavelength (τ) is computed from the model dust concentration (C_{dust}) of the dust bins (j = 1 to 5) for the vertical levels (k = 1 to 40) as a function of the extinction efficiency at 550 nm ($Q_{ext,\,550}$), the effective radius of dust particles (r_{eff}), and the increment of each vertical level (Δz):

$$\tau = \sum_j \sum_k \left(\frac{3}{4} \frac{Q_{ext,550}(j)}{r_{eff}(j)\rho_p(j)} C_{dust}(j,k)\Delta z(k) \right). \quad (9)$$

[53] $Q_{ext,550}$ is calculated from Mie theory assuming spherical particles and using dust refractive indices from

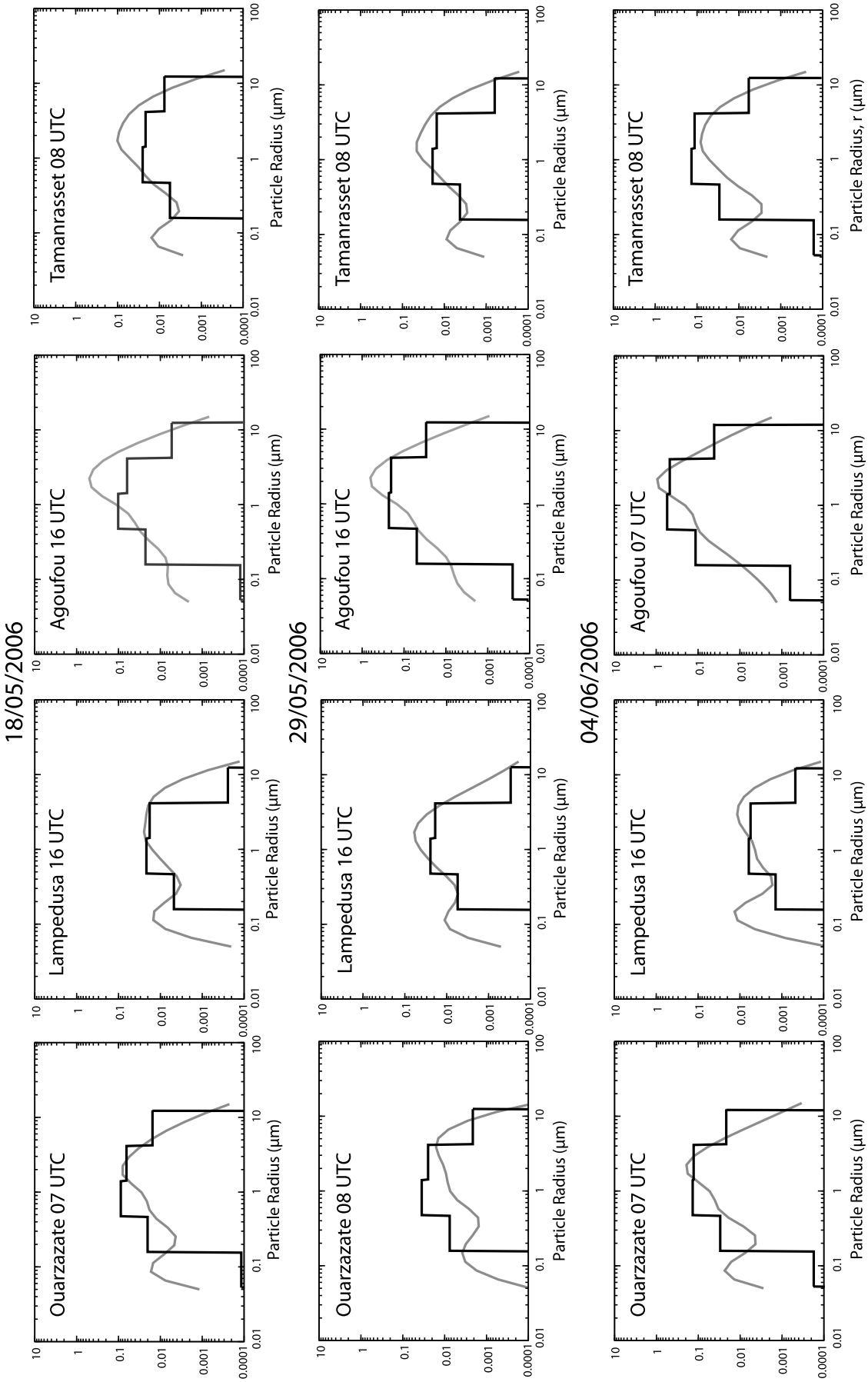

Figure 6. Particle size distributions for the model (black) and derived from AERONET Sun-photometer observations (gray) at four stations located in different transport directions regarding dust source areas (Ouarzazate, 30.9°N, 6.9°W; Lampedusa, 35.5°N, 12.6°E; Agoufou, 15.35°N, 1.5°W; Tamanrasset, 22.8°N, 5.5°E), for chosen days of the studied period when observations were available for the four stations.

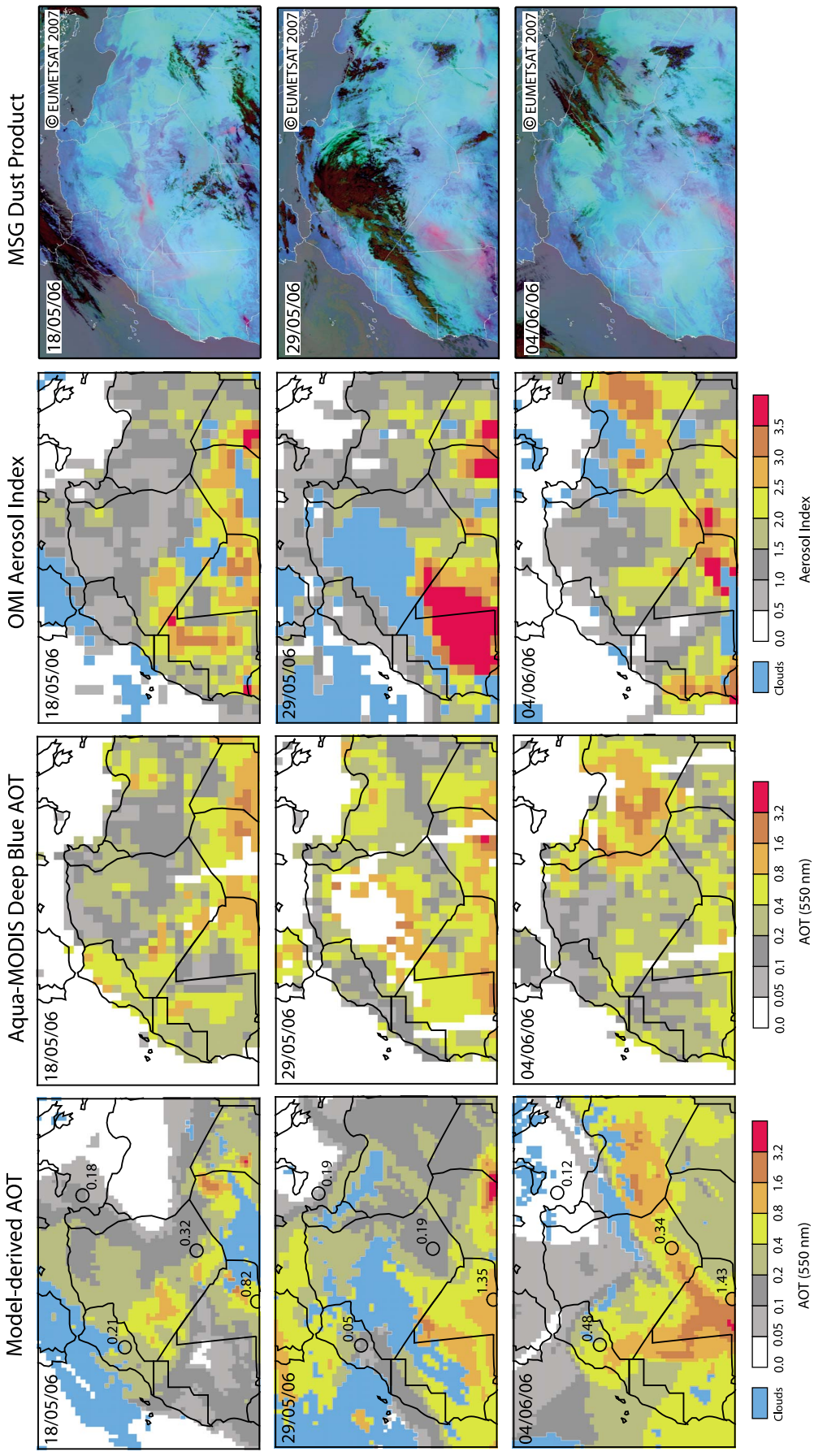

Figure 7. Maps of the horizontal distribution of dust on 18 May, 29 May, and 4 June 2006 around noontime: (left) model-derived aerosol optical thickness at 550 nm; (middle left) Aqua-MODIS Deep Blue aerosol optical thickness at 550 nm; (middle right) OMI aerosol index; (right) MSG dust product. In MSG images, magenta colors indicate dust, dark red colors cold, thick high-level clouds and brown colors thick midlevel clouds. Aerosol optical thickness measured at 440 nm at noontime for four AERONET sites (Ouarzazate, Lampedusa, Tamanrasset, and Agoufou) are reported on model-derived AOT maps.

Sinyuk et al. [2003]. It is 0.31 for the smallest dust bin, and 3.04, 2.43, 2.25, and 2.11 for the larger dust bins, respectively.

[54] On 18 May, the model simulates correctly the AOT values in the Bodélé region, Niger, eastern Mali, southern Algeria, and west of the Tademait Plateau compared with both Aqua-MODIS and OMI dust products. The same general patterns are observed on the MSG images. Magenta dust plumes are observed over the Bodélé and a spot in eastern Niger. Larger plumes are observed over southern Algeria and the border between Mali and Niger, central Algeria, and at the border between Mauritania and Algeria. However, the model underestimates the AOT by at least a factor of 2 over Mauritania compared with Aqua-MODIS Deep Blue AOT. It can be noticed that the information concerning dust load over northern Morocco and eastern Libya differs from one satellite product to the others. On 29 May, the model simulates the highest AOT east of the Bodélé area, where high Aqua-MODIS Deep Blue AOT and OMI AI are observed. The location and the intensity of the AOT values correspond to the satellite observations over Mauritania, Mali, Niger, and western Algeria. Aqua-MODIS Deep Blue AOT over Spain due to transported dust are well captured by the model but are not pointed out by the OMI AI. In contrast, lower AOT are simulated over Libya as well as observed by OMI but not by Aqua-MODIS. Compared with model results and Aqua-MODIS products, the OMI AI are very high over western Mali and Mauritania. Finally, on 4 June, the main areas with high AOT are simulated and observed in Mali and Libya by the model and the satellite products but with different relative intensities. Both model and Aqua-MODIS AOT are quite low in the Bodélé, whereas the OMI AI is relatively higher. In contrast, in Tunisia and northeastern Algeria, the Aqua-MODIS Deep Blue AOT is quite high, whereas both simulations and OMI AI indicate no or very low dust loads. The MSG magenta dust plumes are observed over Mali and Mauritania, at the border between Morocco and Algeria and over Libya. The main regions where simulations show high AOT values generally correspond spatially to the ones with high Aqua-MODIS Deep-Blue AOT and/or OMI AI. With the MSG images it is not possible to obtain quantitative information. It is difficult to conclude on the relative strength of the identified dusty places from the different derived-satellite products. Indeed, they sometimes point out different areas with high dust load contents. Further investigations have to be done to compare model AOT outputs and satellite dust products directly.

[55] On the model-derived AOT maps, the AERONET AOT measurements at 440 nm are also reported for the four sites Ouarzazate, Lampedusa, Tamanrasset, and Agoufou. To compare the model-derived AOT and the measurements, we have to keep in mind that they are not measured and computed at the same wavelengths. Nevertheless, the model simulations reproduce well both the spatial and temporal variability and the order of magnitude of the local measured aerosol optical thicknesses. For the four stations, the minima and maxima are measured and simulated on the same days. We can also notice that our results are consistent. In fact, a good match between simulated and AERONET size distributions (Figure 6) also implies a good match between simulated and AERONET AOT (Figure 7).

[56] Moreover, the simulated vertical distribution of dust plume is evaluated using model results presented by *Heinold et al.* [2009] and airborne vertical measurements performed during the SAMUM-1 campaign [*Esselborn et al.*, 2009]. Following *Heinold et al.* [2009], a lidar ratio of 55 sr is used for the computation of the backscatter coefficient (Figure 8). The Falcon flight tracks are presented in Figure 1. On 20 May, the cross section of the lidar backscatter measurements shows a maximum in the dust layer on the northwestern side of the Atlas between 1.5 and 2.5 km height (Figure 8c1). This dust layer comes from Mali and Mauritania. *Heinold et al.* [2009] overpredicted this dust layer (Figure 8a), whereas the new simulated backscatter coefficients (Figure 8c) match the measurements. South of the Atlas Mountains an elevated dust layer around 5 km in height is measured by the lidar. As for the previous model study, we underestimate the dust load content at this altitude, and we are still not able to model this transported dust plume satisfyingly. This may be explained by the fact that dust emissions and/or dust advection and transport are not yet adequately represented in the model for this case. On 4 June, the dust maximum is measured around 3 km height in the south of the Atlas Mountains (Figure 8f). This maximum is now well reproduced using the new model developments (Figure 8d), whereas it is not caught on Figure 8b. In the model results, the surface dust observed is nevertheless always slightly underestimated south of the Atlas. North of the Atlas, the new dust distribution is overestimated compared with the previous simulations by *Heinold et al.* [2009] and the measurements. This could partly be explained by too strong emissions or by how the dust is transported over the Atlas. In fact, in Figure 7, the simulated plume on 4 June is more developed over the Atlas Mountains than the MODIS and the OMI aerosol plumes. We have also to consider the influence of the topography on the evolution of the plume. This variation along the path may be attributed to the influence of the topography. The model topography (Figure 8d) appears to be a little bit smoother than the real topography (Figure 8f). This can maybe contribute to an easier transport of the plume from one side to the other side of the Atlas in the model as compared with the measurements. In this area, the downward mixing of dust is, however, well simulated by the model.

4.2.3. Dry and Wet Deposition During the SAMUM-1 Period

[57] Dust deposition by sedimentation or scavenging strongly depends on dust properties (nonlinear size-dependent processes), of transport dynamics and meteorological conditions. At the present time, an evaluation of the model dust deposition remains difficult owing to the locations and periods for which in situ observations are available. For example, *Mahowald et al.* [1999] presented a compilation of dust indicators and records from a terrestrial and marine paleoenvironment database. Annual fluxes to marine sediments range over several orders of magnitude from 0.2 to 141.6 g m^{-2} yr^{-1} and from 0.8 to 27.4 g m^{-2} yr^{-1} for eolian fluxes to sediment traps. The large dust deposition variability observed can be explained by the different areas and periods studied and also by the different measurement methods used. For North Africa, *Mahowald* [2007] reported the annual deposition flux from a model: dust flux can range from 10 to several hundreds of g m^{-2} yr^{-1} over the Sahara,

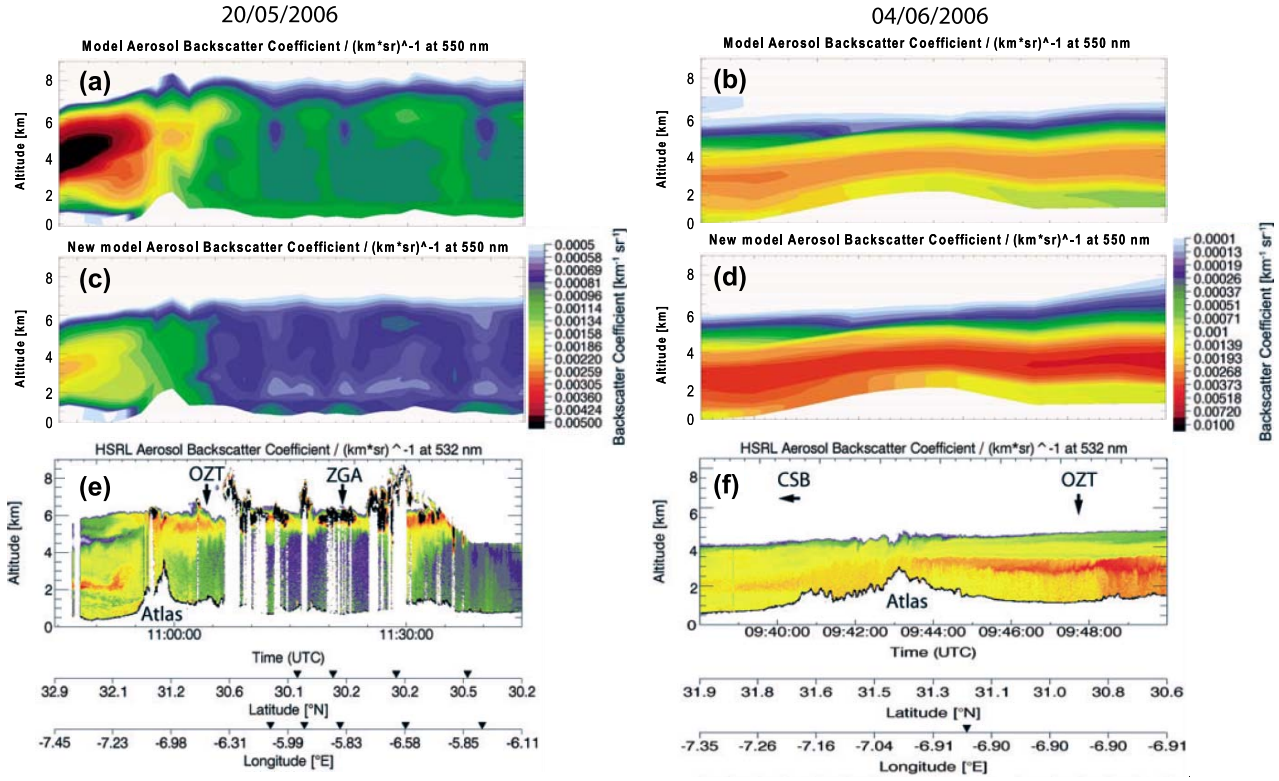

Figure 8. Cross section of dust backscatter coefficient computed by *Heinold et al.* [2009] (Figure 8a), this study (Figure 8c), and measured by HSRL lidar during Falcon flights [*Esselborn et al.*, 2009] from Casablanca to Ouarzazate (OZT) via Zagora (ZGA) on 20 May 2006 (1045–1145 UTC) (Figure 8e). Same information from Casablanca (CSB) to Ouarzazate (OZT) on 4 June 2006 (0918–1034 UTC) (Figures 8b, 8d, and 8f, respectively). The Falcon flight tracks are shown in Figure 1. Arrows on the longitude/latitude axis indicate changes in the flight direction of the aircraft as presented by *Heinold et al.* [2009].

and downwind the North African dust sources' dust deposition flux over the Atlantic can range from 5 to several tens of g m^{-2} yr^{-1}. *Goudie and Middleton* [2001] gathered estimates of rates of dust deposition for sites at varying distances from the Sahara. As might be expected, there is a tendency for rates to be lowest at large distances from potential sources. *McTainsh et al.* [1997] also investigated the dust deposition and particle size in Mali for the southern Saharan margin. Because no deposition measurements were available for the SAMUM-1 period, we only present how the dust deposition is simulated in the model for a real case simulation over the continent and the close marine areas (Figures 9a and 9b).

[58] For the studied period, most of the simulated dry deposition occurs in the vicinity and downwind from the dust source areas (middle east and west Algeria, southwestern Algeria, Libya, Bodélé, and Mali). The Atlantic in the vicinity of the continent and the western part of the Mediterranean Sea are the main areas for dry deposition of dust in marine areas. The wet deposition is very high in middle and western Algeria and in northeastern Morocco, where high precipitation rates are simulated during strong convective events. The wet scavenging is also efficient over west and central Libya, and in the east of Mali, south of the Adrar Iforas. For the North Atlantic Ocean in the vicinity of the Moroccan coast and for the west and central Mediterranean Sea, the simulated wet scavenging is more efficient than the dry deposition process.

[59] The ratio between the deposition (dry, wet, and sum) and the emission for each of the five model dust bins and for the complete model dust size range is reported in Table 4. About 67% of the emitted dust is deposited over the area shown in Figure 9, and almost 33% of the emitted dust is transported out of this area (Table 4). As we do not consider in this study the deposition of the intercontinental long-range transport particles over the Atlantic, the dry deposition is relatively higher than the wet deposition. The dry deposition is the major model depletion process for the large particles (8–24 μm in diameter). It is also relatively high for the particles between 2.7 and 8 μm in diameter and for the very fine ones (with a diameter between 0.1 and 0.3 μm). The dry scavenging is as efficient as the wet scavenging for the particles ranging from 2.7 to 8 μm in diameter, whereas the wet scavenging is the main process to remove particles ranging from 0.1 to several micrometers from the atmosphere.

5. Conclusions

[60] Simulations of Saharan dust emission, transport, and deposition are performed using new developments of the regional model COSMO-MUSCAT. To have a more physical representation of the dust emissions, more accurate and

Table 4. Deposition Load Versus Emission Load for Dry Deposition, Wet Deposition, and Dry and Wet Deposition Sum[a]

Dust Bin	Dry Deposition/Emission (%)	Wet Deposition/Emission (%)	Dry and Wet Deposition/Emission (%)
1. 0.1–0.3 μm	21.6	32.6	54.2
2. 0.3–0.9 μm	12.5	28.0	40.5
3. 0.9–2.7 μm	8.9	29.2	38.1
4. 2.7–8 μm	29.3	24.7	54.0
5. 8–24 μm	80.3	11.0	91.3
$\sum$ bins 0.1–24 μm	47.9	19.4	67.3

[a]Results are computed for each of the five model dust bins and for the complete model dust size range, for the whole studied area between 10 May and 5 June 2006.

updated surface soil data sets are used and a new representation of the dust size distribution is proposed. Despite current modeling limits and uncertainties, as, for instance, the determination of the binding energies and the modeling of the soil crusting, our model system is based on physics as much as is reasonable, given current data sets and models. The advantage of our approach compared with the previous regional modeling works of *Heinold et al.* [2007, 2009] is that no tuning factor on the erosion thresholds is needed for the whole Sahara. Therefore this should lead to a better representation of reality. Moreover, we pay specific attention to the Bodélé region with regard to the representation of the surface wind [*Laurent et al.*, 2008b] and the emitted dust size distribution [*Todd et al.*, 2007]. Thanks to the unique data set of the BoDEx measurements, we can constrain the model for this very special area.

[61] For the studied period (10 May to 5 June 2006), the SAMUM-1 measurements and satellite and station observations are available to evaluate the relevance of our simulations. In agreement with previous dust load estimations for a comparable time period, 78 Tg of Saharan dust are emitted between 10 May and 5 June. A first complete comparison between simulated dust source areas and dust sources located using a backtracking analysis of MSG dust observations is done. Moreover, complementary information given by surface dust observations from meteorological stations allows us to correctly evaluate the simulated dust emissions. For the five subperiods of the SAMUM-1 campaign, a very good match of the spatiotemporal variability of dust source areas is observed between the location of the simulated intense dust emissions, the MSG source areas, and the dust observations of the stations.

[62] The representation of the dust size distribution is evaluated with regard to SAMUM-1 airborne measurements, model results of *Heinold et al.* [2009], and AERONET inversion products. The relative intensity and the temporal variability of the dust size distribution due to dust transported from different sources are well matched by the model for different sites located in the SAMUM-1 area, in the Mediterranean Sea, in middle Algeria, and at the limit between the southern Sahara and Sahel. The obtained concurrence supports the fact that the model dust size distribution is simulated realistically.

[63] As the location of the main source areas and the dust size distribution well concur with observations and measurements, we go further in the evaluation of our simulations comparing the horizontal distribution of the model-derived AOT with Aqua-MODIS Deep-Blue AOT and OMI AI. The main simulated regions with high AOT values generally match those of the Aqua-MODIS Deep-Blue AOT and/or the OMI AI. These two satellite-derived products sometimes point out different areas with high dust load content, making

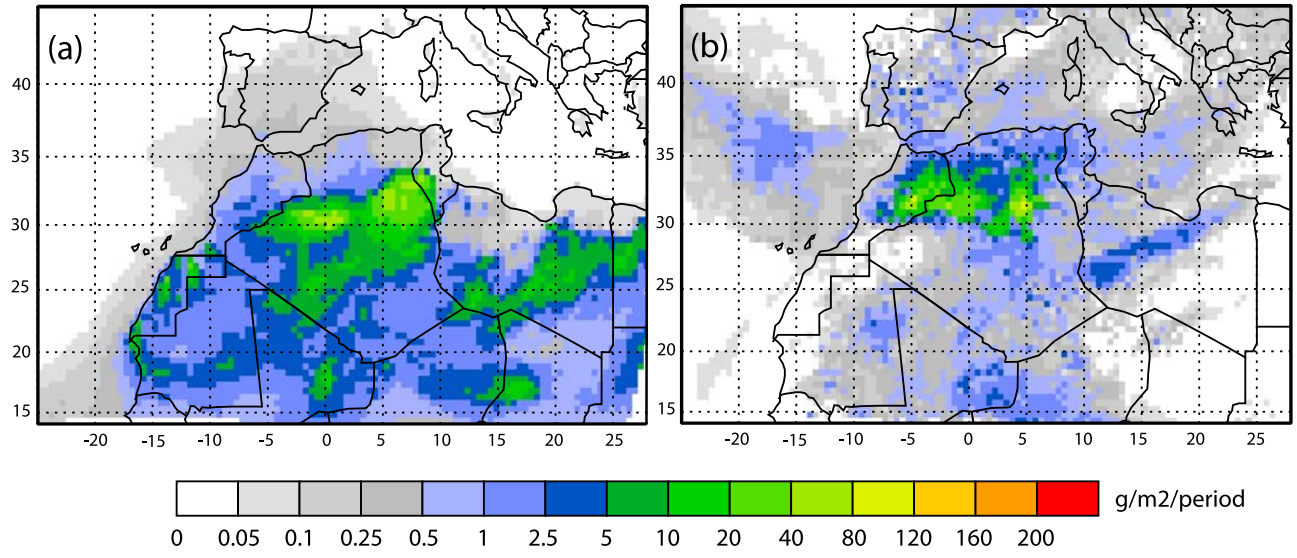

Figure 9. Map of the (a) total dry deposition and (b) the total wet deposition computed for the studied area between 10 May and 5 June 2006.

the direct comparison tricky. Moreover, the simulated vertical distribution of dust plume is evaluated using the model results of *Heinold et al.* [2009] and airborne vertical measurements performed during the SAMUM-1 campaign. For the studied cases, the locations of the maxima of the dust layers better correspond to the measurements than do the former model results. However, for 20 May we are still not able to model transported dust plume satisfyingly. This may be because dust emissions and/or dust advection and transport are not yet adequately represented in the model for this case. In general, our dust simulations match the SAMUM-1 airborne measurements as well as the results presented by *Heinold et al.* [2009]. This constitutes a clear improvement of the dust simulations, as we do not use a tuning factor on the erosion thresholds for the Sahara as formerly done.

[64] Finally, the dry and wet dust deposition patterns are studied. Two thirds of the dust is deposited in the vicinity of the emitted source areas over North Africa and close marine areas, and 33% is transported toward other continents and remote ocean areas. Most of the simulated dry deposition occurs in the vicinity of, and immediately downwind of, the dust source areas (middle east and west Algeria, southwestern Algeria, Libya, Bodélé, and Mali). The highest wet deposition fluxes are simulated in middle and western Algeria and in northeastern Morocco where high precipitation rates are simulated during strong convective events. With regard to the oceanic deposition areas, the simulated wet scavenging is more efficient than the dry deposition process for the North Atlantic Ocean in the vicinity of the Moroccan coast and for the west and central Mediterranean Sea.

[65] Our modeling approach, based on a more accurate and updated surface soil database and using SAMUM-1 measurements as well as satellite and stations observations ensures as well as possible the quality of the Saharan dust simulations. However, for some events, the transported dust plumes are still not correctly represented. Meteorological dynamics appear in these cases as a limiting factor to correctly reproduce the dust load as well as the vertical advection and horizontal distributions. To improve the simulation of such dust events, detailed investigations concerning the meteorological fields should be done. It is also worth noting that the dynamics of the surface should be characterized in future studies.

[66] **Acknowledgments.** B. Laurent is funded by the Deutsche Forschungsgemeinschaft (DFG) (project LA 2583/1–1). This work contributes to the project SAMUM funded by the DFG (FOR 539). We thank Andreas Petzold (Deutsches Zentrum für Luft- und Raumfahrt, Institut für Physik der Atmosphäre) for the use of the airborne measurements performed during SAMUM-1. We thank A. Ansmann, J. Cuesta, P. Goloub, S. Pugnaghi, R. Santangelo, and the AERONET teams for their efforts in establishing and maintaining the sites and for kindly providing data. MSG images were kindly provided by EUMETSAT. Aqua-MODIS AOT and OMI AI data used in this study were produced with the Giovanni online data system, developed and maintained by the NASA Goddard Earth Sciences (GES) Data and Information Services Center (DISC). We are grateful to the referees for their constructive and helpful comments.

References

Ackerman, S. A. (1997), Remote sensing aerosols using satellite infrared observations, *J. Geophys. Res.*, *102*(D14), 17,069–17,079, doi:10.1029/96JD03066.

Alfaro, S. (2007), Influence of soil texture on the binding energies of fine mineral dust particles potentially released by wind erosion, *Geomorphology*, *93*, 157–167.

Alfaro, S., A. Gaudichet, L. Gomes, and M. Maillé (1997), Modeling the size distribution of a soil aerosol produced by sandblasting, *J. Geophys. Res.*, *102*, 11,239–11,249, doi:10.1029/97JD00403.

Alfaro, S., A. Gaudichet, L. Gomes, and M. Maillé (1998), Mineral aerosol production by wind erosion: Aerosol particles size and binding energies, *Geophys. Res. Lett.*, *25*, 991–994, doi:10.1029/98GL00502.

Alfaro, S., and L. Gomes (2001), Modeling mineral aerosol production by wind erosion: Emission intensities and aerosol size distributions in source areas, *J. Geophys. Res.*, *106*, 18,075–18,084, doi:10.1029/2000JD900339.

Alfaro, S., J. L. Rajot, and W. G. Nickling (2004), Estimation of PM_{20} emissions by wind erosion: Main sources of uncertainties, *Geomorphology*, *59*, 63–74.

Balkanski, Y., D. Jacob, G. Gardner, W. Graustein, and K. Turekian (1993), Transport and residence times of tropospheric aerosols inferred from a global three-dimensional simulation of ^{210}Pb, *J. Geophys. Res.*, *98*(D11), 20,573–20,586, doi:10.1029/93JD02456.

Ballantine, J. A., G. S. Okin, D. E. Prentiss, and D. A. Roberts (2005); Mapping North African landforms using continental scale unmixing of MODIS imagery, *Remote Sens. Environ.*, *97*, 470–483.

Bauer, S. E., Y. Balkanski, M. Schulz, D. A. Hauglustaine, and F. Dentener (2004), Global modeling of heterogeneous chemistry on mineral aerosol surfaces: The influence on tropospheric ozone chemistry and comparison to observations, *J. Geophys. Res.*, *109*, D02304, doi:10.1029/2003JD003868.

Belnap, J., S. L. Phillips, and M. E. Miller (2004) Response of desert biological soil crusts to alterations in precipitation frequency, *Oecologia*, *141*, 306–316, doi:10.1007/s00442-003-1438-6.

Bergametti, G., E. Remoudaki, R. Losno, E. Steiner, B. Chatenet, and P. Buat-Ménard (1992), Sources, transport and deposition of atmospheric phosphorus over the northwestern Mediterranean, *J. Atmos. Chem.*, *14*, 501–513.

Bergametti, G., B. Marticorena, and B. Laurent (2007), Key processes for dust emissions and their modeling, in *Regional Climate Variability and Its Impacts in the Mediterranean Area*, *NATO Sci. Ser. IV*, *Earth Environ. Sci.*, vol. 79, edited by A. Mellouki and A. R. Ravishankara, pp. 63–81, Springer, Dordrecht, Netherlands.

Bouet, C., G. Cautenet, R. Washington, M. C. Todd, B. Laurent, B. Marticorena, and G. Bergametti (2007), Mesoscale modeling of aeolian dust emission during the BoDEx 2005 experiment, *Geophys. Res. Lett.*, *34*, L07812, doi:10.1029/2006GL029184.

Callot, Y., B. Marticorena, and G. Bergametti (2000), Geomorphologic approach for modelling the surface features of arid environments in a model of dust emissions: application to the Sahara desert, *Geodin. Acta*, *13*, 245–270.

Chappell, A., A. Warren, A. O'Donoghue, A. Robinson, A. D. Thomas, and C. S. Bristow (2008), The implications for dust emission modelling of spatial and vertical variations in horizontal dust flux and particle size in the Bodélé Depression, northern Chad, *J. Geophys. Res.*, D04214, doi:10.1029/2007JD009032.

Chatenet, B., B. Marticorena, L. Gomes, and G. Bergametti (1996), Assessing the microped size distributions of desert soils erodible by wind, *Sedimentology*, *43*, 901–911.

Chepil, W. S. (1945), Dynamics of wind erosion, *Soil Sci.*, *60*, 305–320.

D'Almeida, G. A. (1986), A model for Saharan dust transport, *J. Clim. Appl. Meteorol.*, *25*, 903–916.

Dubovik, O., et al. (2006), Application of spheroid models to account for aerosol particle nonsphericity in remote sensing of desert dust, *J. Geophys. Res.*, *111*, D11208, doi:10.1029/2005JD006619.

Eck, T. F., P. K. Bhartia, P. H. Hwang, and L. L. Stowe (1987), Reflectivity of Earth's surface and clouds in ultraviolet from satellite observations, *J. Geophys. Res.*, *92*(D4), 4287–4296, doi:10.1029/JD092iD04p04287.

Engelstaedter, S., I. Tegen, and R. Washington (2006), North African dust emissions and transport, *Earth Sci.Rev.*, *79*, 73–100, doi:10.1016/j.earscirev.2006.06.004.

Esselborn, M., M. Wirth, A. Fix, B. Weinzierl, K. Rasp, M. Tesche, and A. Petzold (2009), Spatial distribution and optical properties of Saharan dust observed by airborne high spectral resolution lidar during SAMUM 2006, *Tellus, Ser. B*, *61*, 131–143, doi:10.1111/j.1600-0889.2008.00394.x.

Foret, G., G. Bergametti, F. Dulac, and L. Menut (2006), An optimized particle size bin scheme for modeling mineral dust aerosol, *J. Geophys. Res.*, *111*, D17310, doi:10.1029/2005JD006797.

Gillette, D. A. (1979), Environmental factors affecting dust emission by wind erosion, in *Saharan Dust*, edited by C. Morales, pp. 71–94, John Wiley, New-York.

Gillette, D. A., and P. H. Stockton (1989), The effect of nonerodible particles on wind erosion of erodible surfaces, *J. Geophys. Res.*, *94*, 12,885–12,893, doi:10.1029/JD094iD10p12885.

Ginoux, P., J. M. Prospero, O. Torres, and M. Chin (2004), Long-term simulation of global dust distribution with the GOCART model: Correlation with North Atlantic oscillation, *Environ. Modell. Software*, *19*(2), 113–128.

Gomes, L., J. L. Rajot, S. C. Alfaro, and A. Gaudichet (2003), Validation of a dust production model from measurements performed in semi-arid agricultural areas of Spain and Niger, *Catena*, *52*, 257–271.

Goudie, A. S., and N. J. Middleton (2001), Saharan dust storms: Nature and consequences, *Earth Sci. Rev.*, *56*(1–4), 179–204.

Grini, A., G. Myhre, C. S. Zender, and I. S. A. Isaksen (2005), Model simulations of dust sources and transport in the global atmosphere: Effects of soil erodibility and wind speed variability, *J. Geophys. Res.*, *110*, D02205, doi:10.1029/2004JD005037.

Heinold, B., J. Helmert, O. Hellmuth, R. Wolke, A. Ansmann, B. Marticorena, B. Laurent, and I. Tegen (2007), Regional modeling of Saharan dust events using LM-MUSCAT: Model description and case studies, *J. Geophys. Res.*, *112*, D11204, doi:10.1029/2006JD007443.

Heinold, B., I. Tegen, K. Schepanski, and O. Hellmuth (2008), Dust radiative feedback on Saharan boundary layer dynamics and dust mobilization, *Geophys. Res. Lett.*, *35*, L20817, doi:10.1029/2008GL035319.

Heinold, B., et al. (2009), Regional Saharan dust modelling during the SAMUM 2006 campaign, *Tellus, Ser. B*, *61*, 307–324, doi:10.1111/j.1660-0889.2008.00387.

Heintzenberg, J. (2009), The SAMUM-1 experiment over southern Morocco: Overview and introduction, *Tellus Ser. B*, *61*, 2–11, doi:10.1111/j.1600-0889.2008.00403.x.

Helmert, J., B. Heinold, I. Tegen, O. Hellmuth, and M. Wendisch (2007), On the direct and semidirect effects of Saharan dust over Europe: A modeling study, *J. Geophys. Res.*, *112*, D13208, doi:10.1029/2006JD007444.

Herman, J. R., P. K. Bhartia, O. Torres, C. Hsu, C. Seftor, and E. Celarier (1997), Global distribution of UV-absorbing aerosols from Nimbus 7/TOMS data, *J. Geophys. Res.*, *102*, 16,911–16,922, doi:10.1029/96JD03680.

Hsu, N. C., T. Si-Chee, M. D. King, and J. R. Herman (2004), Aerosol properties over bright-reflecting source regions, *IEEE Trans. Geosci. Remote Sens.*, *42*, 557–569.

Iversen, J. D., and B. R. White (1982), Saltation threshold on Earth, Mars and Venus, *Sedimentology*, *29*, 111–119.

Jickells, T. D., et al. (2005), Global iron connections: Between desert dust, ocean biogeochemistry and climate, *Science*, *308*(5708), 67–71.

Kandler, K., et al. (2009), Size distribution, mass concentration, chemical and mineralogical composition, and derived optical parameters of the boundary layer aerosol at Tinfou, Morocco, during SAMUM 2006, *Tellus, Ser. B*, *61*, 32–50, doi:10.1111/j.1600-0889.2008.00385.x.

Kaufman, Y. J., I. Koren, L. A. Remer, D. Tanré, P. Ginoux, and S. Fan (2005), Dust transport and deposition observed from the Terra-Moderate Resolution Imaging Spectroradiometer (MODIS) spacecraft over the Atlantic Ocean, *J. Geophys. Res.*, *110*, D10S12, doi:10.1029/2003JD004436.

Knippertz, P., C. Deutscher, K. Kandler, T. Müller, O. Schulz, and L. Schütz (2007), Dust mobilization due to density currents in the Atlas region: Observations from the Saharan Mineral Dust Experiment 2006 field campaign, *J. Geophys. Res.*, *112*, D21109, doi:10.1029/2007JD008774.

Knippertz, P., et al. (2009), Dust mobilization and transport in the northern Sahara during SAMUM 2006: A meteorological overview, *Tellus, Ser. B*, *61*, 12–31, doi:10.1111/j.1600-0889.2008.00380.x.

Laurent, B., B. Marticorena, G. Bergametti, and F. Mei (2006), Modeling mineral dust emissions from Chinese and Mongolian deserts, *Global Planet. Change*, *52*(1–4), 121–141.

Laurent, B., B. Marticorena, G. Bergametti, J. F. Léon, and N. M. Mahowald (2008a), Modeling mineral dust emissions from the Sahara desert using new surface and soil developments, *J. Geophys. Res.*, *113*, D14218, doi:10.1029/2007JD009484.

Laurent, B., B. Heinold, I. Tegen, C. Bouet, and G. Cautenet (2008b), Surface wind accuracy for modeling mineral dust emissions: Comparing two regional models in a Bodélé case study, *Geophys. Res. Lett.*, *35*, L09804, doi:10.1029/2008GL033654.

Losno, R., G. Bergametti, P. Carlier, and G. Mouvier (1991), Major ions in marine rainwater with attention to sources of alkaline and acidic species, *Atmos. Environ.*, *25*, 771–777.

Loÿe-Pilot, M. D., J. M. Martin, and J. Morelli (1986), Influence of Saharan dust on the rain acidity and atmospheric input to the Mediterranean, *Nature*, *321*, 427–428.

Mahowald, N. M. (2007), Anthropocene changes in desert area: Sensitivity to climate model predictions, *Geophys. Res. Lett.*, *34*, L18817, doi:10.1029/2007GL030472.

Mahowald, N. M., K. Kohfeld, M. Hansson, Y. Balkanksi, S. P. Harrison, I. C. Prentice, M. Schulz, and H. Rodhe (1999), Dust sources and deposition during the Last Glacial Maximum and current climate: A comparison of model results with paleodata from ice cores and marine sediments, *J. Geophys. Res.*, *104*(D13), 15,895–15,916, doi:10.1029/1999JD900084.

Mahowald, N. M., J. A. Ballantine, J. Feddema, and N. Ramankutty (2007), Global trends in visibility: Implications for dust sources, *Atmos. Chem. Phys.*, *7*, 3309–3339.

Marticorena, B., and G. Bergametti (1995), Modeling the atmospheric dust cycle: 1. Design of a soil derived dust production scheme, *J. Geophys. Res.*, *100*(D8), 16,415–16,430.

Marticorena, B., G. Bergametti, B. Aumont, Y. Callot, C. N'Doumé, and M. Legrand (1997), Modeling the atmospheric dust cycle: 2. Simulations of Saharan dust sources, *J. Geophys. Res.*, *102*(D4), 4387–4404, doi:10.1029/96JD02964.

Marticorena, B., P. Chazette, G. Bergametti, F. Dulac, and M. Legrand (2004), Mapping the aerodynamic roughness length of desert surfaces from the POLDER/ADEOS bi-directional reflectance product, *Int. J. Rem. Sens.*, *25*(3), 603–626.

McTainsh, G. H., W. G. Nickling, and A. W. Lynch (1997), Dust deposition and particle size in Mali, West Africa, *Catena*, *29*, 307–322.

Mei, F., X. Zhang, H. Lu, Z. Shen, and Y. Wang (2004), Characterization of MASDs of surface soils in north China and its influence on estimating dust emission, *Chin. Sci. Bull.*, *49*, 2169–2176.

N'Tchayi, G. M., J. Bertrand, M. Legrand, and J. Baudet (1994), Temporal and spatial variations of the atmospheric dust loading throughout West Africa over the last thirty years, *Ann. Geophys.*, *12*(2–3), 265–273.

N'Tchayi, G. N., J. Bertrand, and S. E. Nicholson (1997), The diurnal and seasonal cycles of wind-borne dust over Africa north of the equator, *J. App. Meteorol.*, *36*(7), 868–882.

Okin, G. S. (2005), Dependence of wind erosion and dust emission on surface heterogeneity: Stochastic modeling, *J. Geophys. Res.*, *110*, D11208, doi:10.1029/2004JD005288.

Okin, G. S., and D. A. Gillette (2001), Distribution of vegetation in wind-dominated landscapes: Implications for wind erosion modeling and landscape processes, *J. Geophys. Res.*, *106*(D9), 9673–9683, doi:10.1029/2001JD900052.

Petzold, A., et al. (2009), Saharan dust absorption and refractive index from aircraft-based observations during SAMUM 2006, *Tellus, Ser. B*, *61*, 118–130, doi:10.1111/j.1600-0889.2008.00383.x.

Prigent, C., I. Tegen, F. Aires, B. Marticorena, and M. Zribi (2005), Estimation of the aerodynamic roughness length in arid and semi-arid regions over the globe with the ERS scatterometer, *J. Geophys. Res.*, *110*, D09205, doi:10.1029/2004JD005370.

Prospero, J. M., P. Ginoux, O. Torres, S. E. Nicholson, and T. E. Gill (2002), Environmental characterization of global sources of atmospheric soil dust identified with the Nimbus 7 Total Ozone Mapping Spectrometer (TOMS) absorbing aerosol product, *Rev. Geophys.*, *40*(1), 1002, doi:10.1029/2000RG000095.

Schepanski, K., I. Tegen, B. Laurent, B. Heinold, and A. Macke (2007), A new Saharan dust source activation frequency map derived from MSG-SEVIRI IR-channels, *Geophys. Res. Lett.*, *34*, L18803, doi:10.1029/2007GL030168.

Schepanski, K., I. Tegen, M. C. Todd, B. Heinold, G. Bönisch, B. Laurent, and A. Macke (2009a), Meteorological processes forcing Saharan dust emission inferred from MSG-SEVIRI observations of subdaily dust source activation and numerical models, *J. Geophys. Res.*, *114*, D10201, doi:10.1029/2008JD010325.

Schepanski, K., I. Tegen, and A. Macke (2009b) Saharan dust transport and deposition towards the tropical northern Atlantic, *Atmos. Chem. Phys.*, *9*, 1173–1189.

Schulz, M., Y. Balkanski, W. Guelle, and F. Dulac (1998), Role of aerosol size distribution and source location in a three-dimensional simulation of a Saharan dust episode tested against satellite-derived optical thickness, *J. Geophys. Res.*, *103*(D9), 10,579–10,592, doi:10.1029/97JD02779.

Shao, Y. (2001), A model for mineral dust emission, *J. Geophys. Res.*, *106*(D17), 20,239–20,254, doi:10.1029/2001JD900171.

Sinyuk, A., O. Torres, and O. Dubovik (2003), Combined use of satellite and surface observations to infer the imaginary part of refractive index of Saharan dust, *Geophys. Res. Lett.*, *30*(2), 1081, doi:10.1029/2002GL016189.

Sokolik, I. N., and O. B. Toon (1999), Incorporation of the mineralogical composition into models of the radiative properties of mineral aerosol from UV to IR wavelengths, *J. Geophys. Res.*, *104*(D8), 9423–9444, doi:10.1029/1998JD200048.

Sow, M., S. C. Alfaro, J. L. Rajot, and B. Marticorena (2009), Size resolved dust emission fluxes measured in Niger during 3 dust storms of the AMMA experiment, *Atmos. Chem. Phys.*, *9*, 3881–3891.

Steppeler, J., G. Doms, U. Schättler, H. W. Bitzer, A. Gassmann, U. Damrath, and G. Gregoric (2003), Meso-gamma scale forecasts using the nonhydrostatic model LM, *Meteorol. Atmos. Phys.*, *82*, 75–96.

Swap, R., M. Garstang, S. Greco, R. Talbot, and J. Y. Gac (1992), Sahara dust in the Amazon basin, *Tellus, Ser. B*, *44*, 133–149.

Tegen, I., S. P. Harrison, K. Kohfeld, I. C. Prentice, M. Coe, and M. Heimann (2002), Impact of vegetation and preferential source areas on global dust aerosol: Results from a model study, *J. Geophys. Res.*, *107*(D21), 4576, doi:10.1029/2001JD000963.

Tegen, I., B. Heinold, M. C. Todd, J. Helmert, R. Washington, and O. Dubovik (2006), Modelling soil dust aerosol in the Bodélé depression during the BoDEx campaign, *Atmos. Chem. Phys.*, *6*, 4345–4359.

Tiedtke, M. (1989), A comprehensive mass flux scheme for cumulus parameterisation in large-scale models, *Mon. Weather Rev.*, *117*, 1779–1799.

Todd, M. C., R. Washington, J. V. Martins, O. Dubovik, G. Lizcano, S. M'Bainayel, and S. Engelstaedter (2007), Mineral dust emission from the Bodélé Depression, northern Chad, during BoDEx 2005, *J. Geophys. Res.*, *112*, D06207, doi:10.1029/2006JD007170.

Todd, M. C., et al. (2008a), Quantifying uncertainty in estimates of mineral dust flux: An intercomparison of model performance over the Bodélé Depression, northern Chad, *J. Geophys. Res.*, *113*, D24107, doi:10.1029/2008JD010476.

Todd, M. C., R. Washington, S. Raghavan, G. Lizcano, and P. Knippertz (2008b), Regional model simulations of the Bodélé low-level jet of northern Chad during the Bodélé Dust Experiment (BoDEx 2005), *J. Clim.*, *21*, 995–1012, doi:10.1175/2007JCLI1766.1.

Torres, O., P. K. Bhartia, J. R. Herman, and Z. Ahmad (1998), Derivation of aerosol properties from satellite measurements of backscattered ultraviolet radiation: Theoretical basis, *J. Geophys. Res.*, *103*, 17,099–17,110, doi:10.1029/98JD00900.

Tsyro, S., and L. Erdman (2000), Parameterisation of aerosol deposition processes in EMEP MSC-E and MSC-W transport models, *EMEP/MSC-W Note 7/00*, Norw. Meteorol. Inst., Oslo.

Warren, A., A. Chappell, M. C. Todd, C. Bristow, N. Drake, S. Engelstaedter, V. Martins, S. M'bainayel, and R. Washington (2007), Dust-raising in the dustiest place on earth, *Geomorphology*, *92*(1–2), 25–37.

Weinzierl, B., A. Petzold, M. Esselborn, M. Wirth, K. Rasp, K. Kandler, L. Schütz, P. Koepke, and M. Fiebig (2009), Airborne measurements of dust layer properties, particle size distribution and mixing state of Saharan dust during SAMUM 2006, *Tellus, Ser. B*, *61*, 96–117, doi:10.1111/j.1600-0889.2008.00392.x.

Wolke, R., O. Hellmuth, O. Knoth, W. Schröder, B. Heinrich, and E. Renner (2004a), The chemistry-transport modeling system LM-MUSCAT: Description and CityDelta applications, in *Air Pollution Modeling and Its Application XVI*, edited by C. Borrego and S. Incecik, pp. 427–437, Kluwer Acad., New York.

Wolke, R., O. Hellmuth, O. Knoth, W. Schröder, and E. Renner (2004b), The parallel model system LM-MUSCAT for chemistry transport simulations: Coupling scheme, parallelization and application, in *Parallel Computing: Software Technology*, *Algorithms*, *Architectures*, *and Applications*, pp. 363–370, Elsevier, Amsterdam.

Zender, C. S., H. Bian, and D. Newman (2003), Mineral Dust Entrainment and Deposition (DEAD) model: Description and 1990s dust climatology, *J. Geophys. Res.*, *108*(D14), 4416, doi:10.1029/2002JD002775.

Zhang, L., S. Gong, J. Padro, and L. Barrie (2001), A size-segregated particle dry deposition scheme for an atmospheric aerosol module, *Atmos. Environ.*, *35*, 549–560.

M. Esselborn, European Southern Observatory, Karl-Schwarzchild-Strasse 2, D-85748 Garching, Germany.

B. Heinold and I. Tegen, Leibniz-Institut für Troposhärenforschung, Permoserstrasse 15, D-04318 Leipzig, Germany.

B. Laurent, Laboratoire Interuniversitaire des Systèmes Atmosphériques, 61 Avenue de Général de Gaulle, 94010 Créteil Cedex, France. (benoit.laurent@lisa.u-pec.fr)

K. Schepanski, Institute for Atmospheric Science, School of Earth and Environment, University of Leeds, Leeds LS2 9JT, UK.

B. Weinzierl, Deutsches Zentrum für Luft- und Raumfahrt, Institut für Physik der Atmosphäre, Münchnerstrasse 20, D-82234 Oberpfaffenhofen, Germany.